JCI The Journal of Clinical Investigation

AMPK is necessary for Treg functional adaptation to microenvironmental stress during malignancy and viral pneumonia

Manuel A. Torres Acosta, … , Samuel E. Weinberg, Benjamin D. Singer

J Clin Invest. 2025. https://doi.org/10.1172/JCI179572.

Research In-Press Preview Immunology Oncology Pulmonology

Graphical abstract

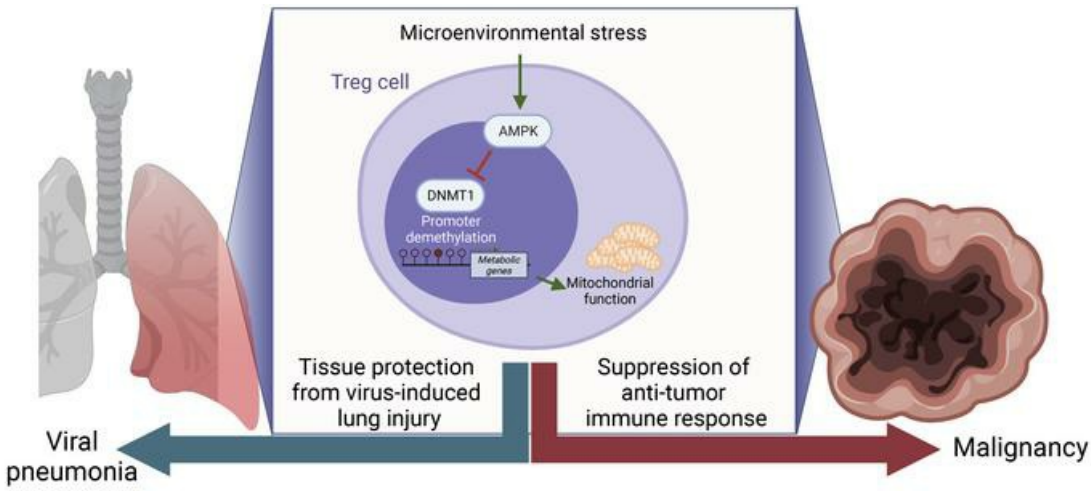

AMPK is necessary for Treg functional adaptation to microenvironmental stress during malignancy and viral pneumonia

Manuel A. Torres Acosta[1,2,3], Jonathan K. Gurkan[1,2,3], Qianli Liu[1,3], Nurbek Mambetsariev[4], Carla P. Reyes Flores[1,3], Kathryn A. Helmin[1], Anthony M. Joudi[1], Luisa Morales-Nebreda[1], Kathleen Cheng[2,3,5], Hiam Abdala-Valencia[1], Samuel E. Weinberg[6,†], and Benjamin D. Singer[1,7,8,9,†,*]

[1]Division of Pulmonary and Critical Care Medicine, Northwestern University Feinberg School of Medicine, Chicago, IL USA

[2]Medical Scientist Training Program, Northwestern University Feinberg School of Medicine, Chicago, IL USA

[3]Driskill Graduate Program, Northwestern University Feinberg School of Medicine, Chicago, IL USA

[4]Division of Allergy and Immunology, Northwestern University Feinberg School of Medicine, Chicago, IL USA

[5]Department of Dermatology, Northwestern University Feinberg School of Medicine, Chicago, IL USA

[6]Department of Pathology, Northwestern University Feinberg School of Medicine, Chicago IL USA

[7]Department of Biochemistry and Molecular Genetics, Northwestern University Feinberg School of Medicine, Chicago, IL USA

[8]Simpson Querrey Institute for Epigenetics, Northwestern University Feinberg School of Medicine, Chicago, IL USA

[9]Simpson Querrey Lung Institute for Translational Science (SQ LIFTS), Northwestern University Feinberg School of Medicine, Chicago, IL USA.

[†] Senior authors contributed equally to this work.

26 *To whom correspondence should be addressed:

27 Benjamin D. Singer, MD

28 Division of Pulmonary and Critical Care Medicine, Department of Medicine

29 Department of Biochemistry and Molecular Genetics

30 Northwestern University Feinberg School of Medicine

31 303 E. Superior St.

32 Simpson Querrey 5th Floor

33 Chicago, IL 60611 USA

34 benjamin-singer@northwestern.edu

35 Tel: (312) 503-4494

36 Fax: (312) 503-0411

37

38 Declaration of interests: NM is currently an employee and owns stock in Vertex Pharmaceuticals. BDS

39 holds United States Patent No. US 10,905,706 B2, Compositions and Methods to Accelerate

40 Resolution of Acute Lung Inflammation, and serves on the Scientific Advisory Board of Zoe

41 Biosciences. The other authors have no competing interests to declare.

Abstract

CD4+FOXP3+ regulatory T (Treg) cells maintain self-tolerance, suppress the immune response to cancer, and protect against tissue injury during acute inflammation. Treg cells require mitochondrial metabolism to function, but how Treg cells adapt their metabolic programs to optimize their function during an immune response occurring in a metabolically stressed microenvironment remains unclear. Here, we tested whether Treg cells require the energy homeostasis-maintaining enzyme AMPK to adapt to metabolically aberrant microenvironments caused by malignancy or lung injury, finding that AMPK is dispensable for Treg cell immune-homeostatic function but is necessary for full Treg cell function in B16 melanoma tumors and during influenza virus pneumonia. AMPK-deficient Treg cells had lower mitochondrial mass and exhibited an impaired ability to maximize aerobic respiration. Mechanistically, we found that AMPK regulates DNA methyltransferase 1 to promote transcriptional programs associated with mitochondrial function in the tumor microenvironment. During viral pneumonia, we found that AMPK sustains metabolic homeostasis and mitochondrial activity. Induction of DNA hypomethylation was sufficient to rescue mitochondrial mass in AMPK-deficient Treg cells, linking AMPK function to mitochondrial metabolism via DNA methylation. These results define AMPK as a determinant of Treg cell adaptation to metabolic stress and offer potential therapeutic targets in cancer and tissue injury.

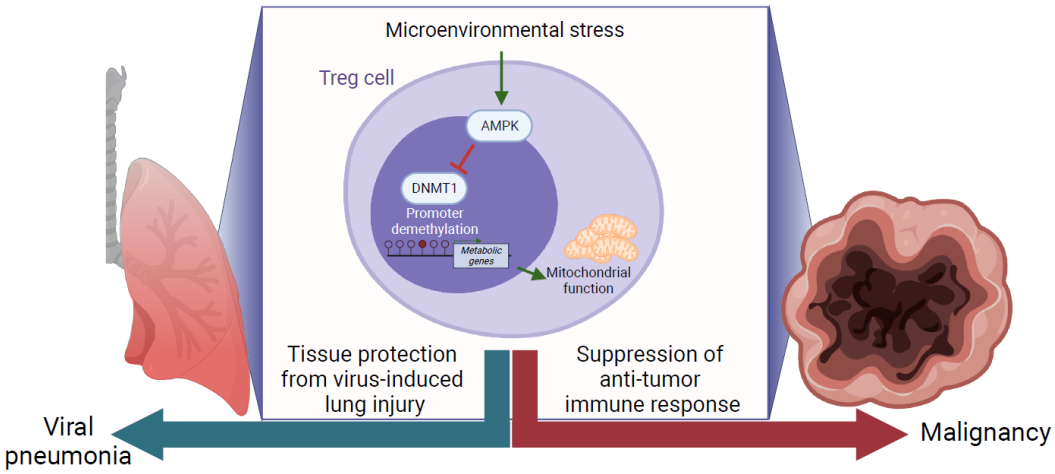

Introduction

Regulatory T (Treg) cells are a subset of CD4+ T cells defined by the expression of the Forkhead box P3 (FOXP3) transcription factor that maintain self-tolerance via the suppression of self-reactive effector immune cells (1, 2). Treg cells also regulate immune responses to cancer and acute inflammatory processes such as infections and tissue injury (3). In the tumor microenvironment (TME), Treg cell-mediated immune suppression becomes maladaptive and dampens the anti-tumor immune response to promote tumor progression (4, 5). In contrast, during acute inflammation such as in viral pneumonia, Treg cells promote tissue protection and recovery by restraining inflammation and coordinating the repair of the injured lung parenchyma (6, 7). Treg cell suppressive function is regulated by cellular metabolism, and while Treg cells upregulate glucose consumption when proliferating, their suppressive function requires oxidative phosphorylation and is dependent on mitochondrial metabolism (8-11). The central role of cellular metabolism in determining Treg cell function has been well described in the TME, where Treg cells rewire their nutrient uptake to adapt to the metabolic aberrations of the microenvironment and thereby sustain their suppressive function (12, 13). Despite the known causal association between cellular metabolism and Treg cell function, how Treg cells sense microenvironmental changes and undergo metabolic adaptation during microenvironmental stress to optimize their suppressive function is unclear.

80

81 AMP-activated protein kinase (AMPK) is a heterotrimeric protein complex that serves as a master
82 regulator of cellular metabolism (14). In settings of energetic stress, adenosine monophosphate (AMP)
83 binds to AMPK and promotes its activation, priming the complex to phosphorylate downstream targets
84 that mediate the restoration of energy homeostasis via one of two α catalytic subunits (AMPKα1,
85 encoded by the *Prkaa1* gene or AMPKα2, encoded by the *Prkaa2* gene) (15, 16). Canonically, AMPK
86 effects its energy-replenishing function through the phosphorylation of cytoplasmic factors; however, in
87 vitro studies support an emerging role for AMPK as a regulator of epigenetic modifiers, including DNA
88 methyltransferase 1 (DNMT1) (17, 18). Whether AMPK activates metabolic transcriptional programs
89 via epigenetic mechanisms in immune cells in vivo remains unknown.

90

91 The two isoforms of the catalytic subunit of AMPK (AMPKα1/α2) are dispensable for in vivo Treg cell-
92 mediated immune self-tolerance, but it is unclear whether Treg cells require AMPKα1/α2 to regulate
93 acute immune responses in metabolically stressed microenvironments (19-22). Considering AMPK's
94 role in sustaining energy homeostasis via the potentiation of mitochondrial metabolism and the
95 necessity of oxidative phosphorylation (OXPHOS) for Treg cell suppressive function, we hypothesized
96 that Treg cells require AMPK during states of metabolic stress to potentiate mitochondrial metabolism
97 and thereby optimize Treg cell suppressive function. To test our hypothesis, we generated Treg cell-
98 specific AMPKα1- and AMPKα2-deficient mice (*Prkaa1*$^{fl/fl}$*Prkaa2*$^{fl/fl}$*Foxp3*$^{YFP\text{-}Cre}$, referred to here as
99 *Prkaa1/2*$^{fl/fl}$*Foxp3*$^{YFP\text{-}Cre}$ mice) and challenged them with either subcutaneous B16 melanoma tumors or
100 intra-tracheal inoculations of influenza A/WSN/33 H1N1 virus, disease models whose outcomes are
101 dependent on Treg cell function and whose microenvironments are burdened with metabolic
102 derangements that challenge cellular metabolism (4, 23). We confirmed that AMPKα1/α2 are
103 dispensable for Treg cell-mediated immune self-tolerance but found that *Prkaa1/2*$^{fl/fl}$*Foxp3*$^{YFP\text{-}Cre}$ mice
104 grew smaller tumors and experienced greater mortality and hypoxemia during influenza, with evidence

105 of greater intra-tumoral and lung immune activation. Mechanistically, loss of AMPKα1/α2 in Treg cells
106 resulted in promoter DNA hypermethylation at specific loci encoding metabolic genes, which were
107 transcriptionally repressed. Consistent with this downregulation of metabolic gene expression,
108 AMPKα1/α2-deficient Treg cells displayed impaired mitochondrial metabolism at homeostasis, in the
109 TME, and in influenza virus-infected lungs. Pharmacological induction of DNA hypomethylation rescued
110 mitochondrial mass in AMPKα1/α2-deficient Treg cells, demonstrating that DNA methylation regulates
111 Treg cell mitochondrial mass in an AMPK-dependent manner. In summary, our data indicate that AMPK
112 is necessary to maintain epigenetic and metabolic programs that support optimal Treg cell suppressive
113 function in metabolically stressed microenvironments, such as the TME and the lung during viral
114 pneumonia.
115
116

Results

AMPKα is dispensable for Treg cell suppressive function under homeostatic conditions. We confirmed loss of AMPKα1/α2 in CD4+*Foxp3*^{YFP}+ Treg cells (see Supplemental Figure 1A for gating strategy) isolated from *Prkaa1/2*$^{fl/fl}$*Foxp3*$^{YFP\text{-}Cre}$ mice, which bred in approximately mendelian sex ratios (Supplemental Figure 1B-E). Consistent with previous reports (19-22), a tissue survey of spleen, thymus, and lungs did not reveal significant differences in CD8+ T cell infiltration between *Prkaa1/2*$^{fl/fl}$*Foxp3*$^{YFP\text{-}Cre}$ and *Prkaa1/2*$^{wt/wt}$*Foxp3*$^{YFP\text{-}Cre}$ (control) mice (Figure 1A). There were no significant differences between *Prkaa1/2*$^{fl/fl}$*Foxp3*$^{YFP\text{-}Cre}$ and control mice in their spleen mass or the relative proportion of naïve (CD62L^{Hi}CD44^{Lo}) and effector (CD62L^{Lo}CD44^{Hi}) splenic conventional T (Tconv) cells (Figure 1B-D), supporting a lack of spontaneous inflammation resulting from Treg cell-specific loss of AMPKα1/α2. Although the total number and proliferation rate of Treg cells was not significantly different between groups (Figure 1E-F), the splenic Treg cell compartment in *Prkaa1/2*$^{fl/fl}$*Foxp3*$^{YFP\text{-}Cre}$ mice displayed a nominal yet statistically significant shift toward a central (CD62L^{Hi}CD44^{Lo}) Treg cell phenotype relative to control mice (Figure 1G). The *Foxp3*$^{YFP\text{-}Cre}$ allele used to drive *Foxp3*-dependent expression of Cre recombinase also drives expression of yellow fluorescent protein (YFP), which serves as a transcriptional reporter for the *Foxp3* locus. Treg cells from *Prkaa1/2*$^{fl/fl}$*Foxp3*$^{YFP\text{-}Cre}$ mice showed similar expression of *Foxp3*-YFP to control mice, although we detected slightly lower FOXP3 protein in AMPKα1/α2-deficient splenic Treg cells measured by direct conjugated antibody staining (Figure 1H-I). AMPKα1/α2-deficient Treg cells displayed no significant differences in their ability to suppress responder CD4+ Tconv cell proliferation in vitro relative to controls (Figure 1J) and showed no significant differences in their surface membrane levels of markers traditionally correlated with Treg cell suppressive function (CD25, CTLA-4, PD-1, TIGIT, and ICOS, Supplemental Figure 1F-J) or their proliferation rate in vitro (Supplemental Figure 1K). Pharmacologic activation of AMPK promotes *Foxp3* expression in vitro (24, 25). To test whether AMPKα1/α2 are

142 necessary for the stability of induced (i)Treg cells in vitro, we subjected CD4+*Foxp3*^{YFP}- Tconv cells
143 sorted from *Prkaa1/2*$^{fl/fl}$*Foxp3*$^{YFP\text{-}Cre}$ and control mice to Treg cell-polarizing conditions for 5 days. We
144 detected no significant difference in *Foxp3* expression between groups after 5 days in culture
145 (Supplemental Figure 1L).
146
147 We also performed unsupervised assessment of the metabolome of AMPKα1/α2-deficient and control
148 splenic Treg cells using liquid chromatography tandem mass spectrometry (LC-MS) but only found 15
149 differentially represented metabolites ($\log_2$ fold change > 0.5, $-\log_{10}$ *p*-value > 1) between groups across
150 the measured metabolites (258 annotated metabolites, Supplemental Figure 1M-N and Supplemental
151 File 1). Finally, we assessed the transcriptional state of AMPKα1/α2-deficient and control splenic Treg
152 cells at homeostasis via RNA-sequencing and identified 78 differentially expressed genes (DEGs)
153 (Figure 1K and Supplemental File 2). Among the genes downregulated in AMPKα1/α2-deficient splenic
154 Treg cells were components of the electron transport chain (*mt-Nd2* and *mt-Co1*) and heat shock
155 proteins (*Hspa1a*, *Hspa1b*, and *Hspa8*), consistent with AMPK's positive regulation of mitochondrial
156 metabolism and the cellular stress response. Genes upregulated in AMPKα1/α2-deficient splenic Treg
157 cells included cytokines and transcription factors associated with effector T cell function (*Tnf*, *Nfkbid*,
158 and *Rora*) and regulators of one-carbon metabolism (*Mthfr*). Gene set enrichment analysis (GSEA)
159 demonstrated downregulation of genes associated with Treg cell identity and function (26) (Figure 1L),
160 suggesting that, although AMPKα1/α2 are dispensable for Treg cell-mediated immune self-tolerance
161 during development and homeostasis, AMPKα1/α2-deficient Treg cells may suffer functional
162 impairment in settings that drive enhanced suppressive function, such as the TME.
163
164 **AMPKα promotes Treg cell suppressive function in the tumor microenvironment.** While we did
165 not detect *Prkaa2* expression in splenic and lymph node Treg cells of mice bearing subcutaneous B16
166 melanoma tumor grafts, we found that control Treg cells upregulated the expression of *Prkaa1* and

167 *Prkaa2* in the TME (Supplemental Figure 2A-B). Hence, to determine whether AMPKα1/α2-deficient
168 Treg cells are functionally impaired in the TME, we challenged *Prkaa1/2*$^{fl/fl}$*Foxp3*$^{YFP\text{-}Cre}$ and control mice
169 with B16 melanoma tumors, finding that *Prkaa1/2*$^{fl/fl}$*Foxp3*$^{YFP\text{-}Cre}$ mice experienced lower tumor volume
170 over time and lower tumor weights at day 15 post-engraftment (Figure 2A-B). Tumors of
171 *Prkaa1/2*$^{fl/fl}$*Foxp3*$^{YFP\text{-}Cre}$ mice had significantly higher CD8-to-Treg cell ratios relative to controls at day
172 15 post-engraftment with a trend toward higher absolute counts of CD8+ Tconv cells in the setting of
173 comparable absolute Treg cell counts, consistent with a loss of Treg cell suppressive function in the
174 TME (Figure 2C-D). We did not find significant differences in the intra-tumor proportion of naïve, central
175 memory, or effector Tconv cell subsets between groups at day 15 post-engraftment (Supplemental
176 Figure 2C-G). There were also no significant differences between the Treg cells of *Prkaa1/2*$^{fl/fl}$*Foxp3*$^{YFP-}$
177 ^{Cre} and control mice in their abundance out of all CD4+ cells or their proportion of central versus effector
178 subsets (Supplemental Figure 2H-J). We assessed the production of interferon gamma (IFN-γ) and
179 tumor necrosis factor-alpha (TNF-α) by tumor-infiltrating CD8+ T cells and found a significantly greater
180 proportion of IFN-γ+CD8+ T cells in tumors of *Prkaa1/2*$^{fl/fl}$*Foxp3*$^{YFP\text{-}Cre}$ mice (Supplemental Figure 2K-
181 L). The proliferation, *Foxp3* gene expression, and FOXP3 protein expression of tumor-infiltrating Treg
182 cells was not significantly different between groups, which was also true for most traditional surface
183 markers of Treg cell suppressive function (Supplemental Figure 2M-T). We leveraged RNA-sequencing
184 to profile the transcriptional state of Treg cells sorted from the tumors of *Prkaa1/2*$^{fl/fl}$*Foxp3*$^{YFP\text{-}Cre}$ and
185 control mice at day 15 post-engraftment and identified 752 DEGs (Figure 2E). Unsupervised clustering
186 revealed that the two largest groups of DEGs (Clusters 1 and 2) were downregulated in AMPKα1/α2-
187 deficient cells (Figure 2F and Supplemental File 3). The *Ppargc1a* gene, encoding the master
188 transcriptional regulator of mitochondrial biogenesis and function, PGC-1α, was significantly
189 downregulated in Cluster 1 in *Prkaa1/2*$^{fl/fl}$*Foxp3*$^{YFP\text{-}Cre}$ mice (Figure 2G). Accordingly, functional
190 enrichment analysis demonstrated that Cluster 1 genes are involved in cellular metabolism and include
191 Gene Ontology (GO) terms relating to cellular response to stress and mitochondrial metabolism; Cluster

192 2 genes are involved in immune effector cell programs and in epigenetic regulation of transcription
193 (Figure 2H). Analysis of Cluster 3 genes, which were upregulated in AMPKα1/α2-deficient Treg cells,
194 linked this cluster to a broad set of cellular functions including negative regulation of transcription. GSEA
195 revealed a positive enrichment of genes associated with allograft rejection and interferon gamma
196 signaling as well as a negative enrichment of genes associated with angiogenesis in tumor-infiltrating
197 AMPKα1/α2-deficient Treg cells (Supplemental Figure 3A-C), consistent with loss of Treg cell function
198 in the TME. In addition, tumor-infiltrating AMPKα1/α2-deficient Treg cells also showed transcriptional
199 signatures associated with downregulated response to hypoxia, glycolysis, and cholesterol
200 homeostasis (Supplemental Figure 3D-F), suggestive of failed metabolic adaptation in the TME.
201 Because *Prkaa1/2*$^{fl/fl}$*Foxp3*$^{YFP\text{-}Cre}$ mice had significantly lower tumor burden relative to control mice at
202 day 15 post-engraftment, we also sorted tumor-infiltrating Treg cells for RNA-sequencing profiling when
203 tumor burden was comparable (day 12 post-engraftment) and identified 427 DEGs (Figure 2I and
204 Supplemental File 4); *k*-means clustering yielded two clusters of genes. Cluster 1 contained genes
205 significantly upregulated in AMPKα1/α2-deficient tumor-infiltrating Treg cells and included genes
206 encoding chemokines (*Ccl2*, *Ccl7*, *Ccl8*), modulators of lipid metabolism (*Cd36, Pparg*, *Lpl, Abca1*),
207 and glycolytic enzymes (*Hk2*, *Hk3*). Cluster 2 represented DEGs downregulated in AMPKα1/α2-
208 deficient tumor-infiltrating Treg cells at day 12 post-engraftment and included *Prkaa1*, along with a
209 variety of Treg cell lineage markers (*Foxp3, Il2ra, Stat5b*) and mediators of Treg cell suppressive
210 function (*Tgfb1*, *Cxcr4*, *Itgae, Ccr8*); notably, Treg cell-specific loss of *Cxcr4* and *Ccr8* are known to be
211 necessary for Treg cell suppressive function in the TME (27, 28). Moreover, GSEA revealed a negative
212 enrichment of genes involved in DNA methylation and histone deacetylation in AMPKα1/α2-deficient
213 tumor-infiltrating Treg cells at day 12 post-engraftment (Figure 2J-K). Collectively, these data indicate
214 that tumor-infiltrating AMPKα1/α2-deficient Treg cells have impaired suppressive function, as
215 evidenced by lower tumor burden over time, higher intra-tumoral CD8-to-Treg cell ratios, and higher
216 frequency of IFN-γ+CD8+ cells in *Prkaa1/2*$^{fl/fl}$*Foxp3*$^{YFP\text{-}Cre}$ mice relative to controls. Our data also

217 suggest that the impaired suppressive function of AMPKα1/α2-deficient Treg cells in the TME is
218 associated with a failure to upregulate metabolic and effector transcriptional programs and that this
219 failed transcriptional adaptation is preceded by an attenuated Treg cell lineage transcriptional program
220 as well as a differential enrichment of expressed genes that regulate epigenetic changes, including
221 DNA methylation.
222
223 **AMPKα2 contributes to the regulation of Treg cell suppressive function in the tumor**
224 **microenvironment.** Previous studies that evaluated the requirement of AMPK for Treg cell-mediated
225 suppression of the anti-tumor immune response leveraged mouse models of Treg cell-specific
226 AMPKα1-conditional knockout mice (*Prkaa1*$^{fl/fl}$*Foxp3*$^{YFP\text{-}Cre}$), and the results have conflicted on whether
227 loss of AMPKα1 potentiates or compromises Treg cell function in the TME (29, 30). To test the
228 relevance of our finding that Treg cells upregulate *Prkaa2* in the TME (see Supplemental Figure 2B),
229 we bred Treg cell-specific AMPKα1-deficient (*Prkaa1*$^{fl/fl}$*Foxp3*$^{YFP\text{-}Cre}$) and AMPKα2-deficient
230 (*Prkaa2*$^{fl/fl}$*Foxp3*$^{YFP\text{-}Cre}$) mice and evaluated their response to B16 melanoma tumor grafts. We observed
231 significantly smaller tumors in Treg cell-specific AMPKα1-deficient mice relative to controls, while those
232 with AMPKα2-deficient Treg cells exhibited significantly greater tumor volume over time through day
233 15 post-tumor engraftment relative to mice bearing control, AMPKα1-, and AMPKα1/α2-deficient Treg
234 cells (Supplemental Figure 4A-B). Consistent with this finding, *Prkaa1*$^{fl/fl}$*Foxp3*$^{YFP\text{-}Cre}$ mice had higher
235 CD8-to-Treg cell ratios compared with *Prkaa2*$^{fl/fl}$*Foxp3*$^{YFP\text{-}Cre}$ and control mice (Supplemental Figure
236 4C). Tumors of *Prkaa2*$^{fl/fl}$*Foxp3*$^{YFP\text{-}Cre}$ mice also exhibited a shift in their CD8+ Tconv cell compartment
237 toward a central memory (CD62L^{Hi}CD44^{Lo}) phenotype (Supplemental Figure 4D-F) and a nominally
238 lower proportion of effector CD4+ Tconv cells relative to *Prkaa1*$^{fl/fl}$*Foxp3*$^{YFP\text{-}Cre}$ and control mice
239 (Supplemental Figure 4G-H). *Prkaa1*$^{fl/fl}$*Foxp3*$^{YFP\text{-}Cre}$ mice had a significantly higher proportion of effector
240 CD8+ T cells (CD62L^{Lo}CD44^{Hi}) relative to *Prkaa2*$^{fl/fl}$*Foxp3*$^{YFP\text{-}Cre}$ mice and had the lowest proportion of
241 Treg cells out of the CD4+ T cell pool in their tumors (Supplemental Figure 4I). Nevertheless, we found

242 no significant differences between groups in the proliferation rate of tumor-infiltrating Treg cells
243 (Supplemental Figure 4J), their FOXP3 and CD25 protein levels measured by flow cytometry
244 (Supplemental Figure 4K-L), and the relative proportion of central versus effector Treg cell subsets
245 (Supplemental Figure 4M). When assessing the status of markers of Treg cell suppressive function, we
246 found that loss of AMPKα1 or AMPKα2 had opposing effects on tumor-infiltrating Treg cell PD-1
247 expression, with loss of AMPKα1 leading to lower levels and loss of AMPKα2 leading to higher levels
248 (Supplemental Figure 4N). To determine the contribution of each AMPKα subunit to the transcriptional
249 signature of AMPKα1/2-deficient Treg cells, we also sorted tumor-infiltrating Treg cells from
250 *Prkaa1*$^{fl/fl}$*Foxp3*$^{YFP\text{-}Cre}$ and *Prkaa2*$^{fl/fl}$*Foxp3*$^{YFP\text{-}Cre}$ mice for RNA-sequencing at day 12 post-engraftment.
251 Treg cells sorted from tumors of *Prkaa1*$^{fl/fl}$*Foxp3*$^{YFP\text{-}Cre}$ and *Prkaa2*$^{fl/fl}$*Foxp3*$^{YFP\text{-}Cre}$ mice only had 29 and
252 35 DEGs relative to controls, respectively (Supplemental Figure 3G-H and Supplemental File 5-6).
253 When compared with the 429 DEGs identified in Treg cells sorted from tumors of *Prkaa1/2*$^{fl/fl}$*Foxp3*$^{YFP\text{-}}$
254 ^{Cre} mice, these data suggest that there is overlap but not complete redundancy in the downstream
255 targets of AMPK complexes occupied by the different AMPKα subunits. GSEA once again revealed
256 differential enrichment of genes associated with DNA methylation relative to controls in Treg cells sorted
257 from tumors of *Prkaa1*$^{fl/fl}$*Foxp3*$^{YFP\text{-}Cre}$ and *Prkaa2*$^{fl/fl}$*Foxp3*$^{YFP\text{-}Cre}$ mice (Supplemental Figure 3I-J),
258 suggesting that both AMPKα subunits contribute to the epigenetic regulation of Treg cells mediated by
259 AMPK complexes.
260
261 **The metabolic landscape of the virus-injured lung resembles the TME in its metabolite**
262 **abundance; however, they differ in the abundance of key carbon sources.** Treg cells must adapt
263 their metabolism to function in the metabolically deranged microenvironment of the TME (31), but it
264 remains undetermined whether other inflammatory microenvironments where Treg cells have critical
265 functions, such as the virally infected lung (32), exhibit similar metabolic aberrations, and thereby
266 present similar environmental stress to Treg cells. To compare the metabolic changes that occur in the

267 TME and the virus-injured lung, we collected interstitial fluid (IF) from mouse lungs 10 days after inf-
268 ection with influenza virus (flu), B16 melanoma tumors 15 days after engraftment, and paired plasma
269 samples. We then measured hydrophilic metabolite abundance via LC-MS. Principal component (PC)
270 analysis of the LC-MS data (303 annotated metabolites) revealed that the first principal component
271 (PC1), which represents 57.9% of the variance in the dataset, captured the variance due to differences
272 in metabolite abundance between flu and tumor IF relative to plasma (Figure 3A-B and Supplemental
273 File 7). Key metabolites that contributed to PC1 include 2-hydroxyglutarate and lactic acid, which are
274 overrepresented in tumor and flu IF relative to plasma (Figure 3C-D) and suggest a state of reduced
275 mitochondrial electron transport chain activity in these disease microenvironments (31). The second
276 principal component (PC2; 14.5% of the variance) was due to differences in metabolite abundance
277 between flu and tumor IF. Interestingly, key carbon sources such as glucose and glutamine were more
278 abundant in flu IF and less abundant in tumor IF relative to plasma (Figure 3E-F). Overrepresentation
279 analysis of the significant differentially represented metabolites in tumor IF relative to plasma (Figure
280 3G and Supplemental Figure 5A-B) and flu IF relative to plasma (Figure 3H and Supplemental Figure
281 5C-D) revealed that the TME and the lung during viral pneumonia undergo significant changes in similar
282 metabolic pathways related to amino acid metabolism (Figure 3I). Nevertheless, direct comparison of
283 tumor IF and flu IF metabolites revealed disease state-specific metabolite signatures, including an
284 enrichment of metabolites related to tryptophan, cysteine, and methionine metabolism in flu IF
285 (Supplemental Figure 6A-D). These data suggest that Treg cells and other immune cells experience
286 shared metabolic challenges in the TME and the injured lung during viral pneumonia but may use
287 different carbon sources in these microenvironments.
288
289 **AMPKα promotes Treg cell tissue-protective function during lung injury from viral pneumonia.**
290 Treg cells provide tissue protection following acute lung injury due to influenza virus infection and other
291 causes of lung pathology and are necessary for resolution of inflammation and repair of lung injury

292 during recovery (32-36). AMPKα1 is required for bulk CD4+ T cell expansion in the lung during viral
293 pneumonia (37), but whether AMPKα1/α2 are necessary for Treg cell function in this context is
294 unknown. We found that AMPKα1/α2-sufficient Treg cells express both *Prkaa1* and *Prkaa2* in lymph
295 nodes and the lung during viral pneumonia (Supplemental Figure 7A-B) and that steady-state splenic
296 AMPKα1/α2-deficient Treg cells have downregulated expression of genes activated during influenza A
297 virus infection (38) (Figure 4A). Considering this transcriptional signature, our findings in the B16
298 melanoma model, and the similarity in interstitial fluid metabolite abundance between flu IF and tumor
299 IF relative to plasma, we hypothesized that Treg cell-specific loss of AMPKα1/α2 would compromise
300 protection from severe viral pneumonia. To test our hypothesis, we challenged *Prkaa1/2*$^{fl/fl}$*Foxp3*$^{YFP\text{-}Cre}$
301 and control mice with intra-tracheal inoculations of influenza virus. *Prkaa1/2*$^{fl/fl}$*Foxp3*$^{YFP\text{-}Cre}$ mice
302 experienced higher mortality, greater weight loss throughout the disease course, and worsened
303 hypoxemia (Figure 4B-D), consistent with a loss of Treg cell tissue-protective function. Accordingly, we
304 detected a significantly greater absolute number of lung CD45+ and CD8+ Tconv cells in
305 *Prkaa1/2*$^{fl/fl}$*Foxp3*$^{YFP\text{-}Cre}$ mice relative to controls at day 10 post-influenza virus inoculation (Figure 4E-
306 F); lung Treg and CD4+ Tconv cell absolute counts were not significantly different between groups
307 (Figure 4G-H). The CD8+ Tconv cell compartment displayed a nominal shift away from an effector
308 phenotype in the lungs of *Prkaa1/2*$^{fl/fl}$*Foxp3*$^{YFP\text{-}Cre}$ mice, but no significant differences were detected in
309 the proportion of other lung CD8+ and CD4+ T cell subsets, including Treg cells (Supplemental Figure
310 7C-J). AMPKα1/α2-deficient Treg cells were less proliferative in the lung at day 10 post-influenza virus
311 inoculation according to Ki-67 expression relative to control Treg cells (Supplemental Figure 7K).
312 Nevertheless, like in our malignancy model, AMPKα1/α2 deficiency did not alter Treg cell *Foxp3*/FOXP3
313 gene/protein expression or the levels of markers associated with Treg cell suppressive function
314 (Supplemental Figure 7L-R).
315

316 As AMPK is a known regulator of cellular metabolism, we assessed the metabolic state of AMPKα1/α2-
317 deficient lung Treg cells during viral pneumonia by performing LC-MS on AMPKα1/α2-sufficient and -
318 deficient Treg cells sorted from lungs at day 10 post-influenza virus inoculation. 159 annotated
319 metabolites were identified (Figure 4I-J and Supplemental File 8), revealing an enrichment of pyruvic
320 acid and lactic acid in AMPKα1/α2-deficient lung Treg cells (Figure 4K-L), metabolites that are upstream
321 of the tricarboxylic acid (TCA) cycle, suggestive of altered mitochondrial metabolism. We also detected
322 depletion of glutathione (GSH), a key antioxidant, in AMPKα1/α2-deficient lung Treg cells (Figure 4M).
323 Overrepresentation analysis of the significantly differentially represented features revealed an
324 overrepresentation of metabolites relating to glycine, serine, and threonine metabolism, glutathione
325 metabolism, and pyruvate metabolism in AMPKα1/α2-deficient Treg cells (Figure 4N). Considering the
326 small number of differentially represented metabolites at homeostasis (15, see Supplemental Figure
327 1M-N), these data suggest AMPK is necessary for Treg cell metabolic adaptation and function during
328 influenza virus pneumonia-induced lung injury.
329
330 **Individual loss of AMPKα2 or AMPKα1 does not compromise Treg cell tissue-protective function**
331 **during lung injury from viral pneumonia.** Considering the dichotomous consequence that individual
332 loss of AMPKα1 versus loss of AMPKα2 had for tumor-infiltrating Treg cell suppressive function, we
333 also evaluated how each AMPKα subunit contributed to Treg cell function during viral pneumonia by
334 challenging *Prkaa1*$^{fl/fl}$*Foxp3*$^{YFP\text{-}Cre}$, *Prkaa2*$^{fl/fl}$*Foxp3*$^{YFP\text{-}Cre}$, and control mice with intra-tracheal
335 inoculations of influenza virus. Survival, weight change, and arterial blood oxygenation over time were
336 similar across all three groups (Supplemental Figure 8A-C). At day 10 post-inoculation, loss of AMPKα2
337 resulted in significantly greater proportions of central memory CD8+ T cells and effector Treg cells but
338 not the frequency of naïve and effector CD8+ T cells, the frequency of naïve and effector CD4+ Tconv
339 cells, the frequency of Treg cells out of total CD4+ cells, or the frequency of central or proliferating Treg
340 cells (Supplemental Figure 8D-L). While lung Treg cells in *Prkaa2*$^{fl/fl}$*Foxp3*$^{YFP\text{-}Cre}$ mice displayed

341 significantly lower proliferation, TIGIT protein expression, and frequency of ICOS^{Hi} Treg cells, the Treg
342 cell protein expression of FOXP3, CD25, PD-1, and CTLA-4 were similar across groups (Supplemental
343 Figure 8M-R). Considering the expression of *Prkaa1* and *Prkaa2* in control Treg cells of influenza-
344 infected lungs (Supplemental Figure 7A-B), as well as the compromised tissue-protective function of
345 AMPKα1/α2-deficient Treg cells during viral pneumonia, these data suggest that AMPKα1 and
346 AMPKα2 share redundant functions in this context.
347
348 **AMPKα is necessary for maximal mitochondrial function in Treg cells.** We demonstrated that
349 mitochondrial metabolism, specifically activity of the electron transport chain, is a key determinant of
350 Treg cell suppressive function (10). To test whether loss of AMPK compromises Treg cell mitochondrial
351 function, we assessed the metabolic status of AMPKα1/α2-deficient and control Treg cells with a
352 metabolic flux assay, finding that AMPKα1/α2-deficient Treg cells have comparable basal oxygen
353 consumption rates (OCR) but significantly lower maximum OCR relative to control Treg cells (Figure
354 5A-C). In fact, AMPKα1/α2-deficient Treg cells were unable to augment their OCR above baseline when
355 challenged with the mitochondrial uncoupling agent carbonyl cyanide m-chlorophenylhydrazone
356 (CCCP). Staining with MitoTracker Deep Red (MitoTracker DR, a dye used to measure mitochondrial
357 mass that is sensitive to mitochondrial membrane potential) revealed lower mitochondrial
358 mass/membrane potential in AMPKα1/α2-deficient Treg cells relative to controls at homeostasis (Figure
359 5D) and in the lung during influenza pneumonia (Figure 5E), consistent with their impaired maximal
360 OCR at homeostasis. AMPK also promotes glycolysis (39); however, the baseline and maximal
361 extracellular acidification rate (ECAR, a measure of glycolytic rate) of AMPKα1/α2-deficient and control
362 Treg cells was comparable between genotypes, suggesting that AMPK is not required to sustain
363 glycolysis in Treg cells at homeostasis (Figure 5F-G). When assessing the individual contribution of the
364 two AMPKα isoforms to mitochondrial mass and metabolism, we found that AMPKα1-deficient Treg
365 cells and AMPKα2-deficient Treg cells had a trend toward lower basal OCR but significantly lower

366 mitochondrial mass in the absence of a basal glycolytic rate defect (Supplemental Figure 9A-C). AMPK
367 also promotes autophagy through inhibition of mammalian target of rapamycin complex 1 (mTORC1)
368 (40, 41), yet we found by flow cytometry that AMPKα1/α2-deficient Treg cells had no significant
369 differences in protein expression of the autophagy marker LC3B (Figure 5H). We further assessed
370 autophagy in splenic AMPKα1/α2-deficient and control Treg cells by measuring colocalization of
371 lysosomal-associated membrane protein 1 (LAMP1) and mitochondria using a LAMP1 fluorochrome
372 and MitoView Green, respectively, as a readout of mitophagy using imaging flow cytometry. We found
373 that AMPKα1/α2-deficient Treg cells had a minimal but significant increase in the co-localization of
374 LAMP-1 and mitochondria, consistent with a nominally significantly greater mitophagy in AMPKα1/α2-
375 deficient Treg cells (Figure 5I). To validate this method for measuring mitophagy, we treated AMPK-
376 sufficient splenic Treg cells with CCCP, the mitochondrial decoupling agent frequently used to induce
377 mitophagy (one of many forms of autophagy) in mammalian cells (42) and measured the change in
378 anti-LAMP-1 fluorochrome mean fluorescence intensity (MFI), MitoView Green MFI, and the mean co-
379 localization between the anti-LAMP-1 fluorochrome and MitoView Green. CCCP treatment decreased
380 the MitoView Green MFI (Supplemental Figure 9D) while increasing the co-localization between anti-
381 LAMP-1 fluorochrome and MitoView Green over time (Supplemental Figure 9E), consistent with an
382 upregulation of mitophagy in the setting of prolonged mitochondrial decoupling. These results
383 collectively suggest that both AMPKα subunits contribute to, and are required for, maximal
384 mitochondrial mass and electron transport chain function in Treg cells.
385
386 **AMPKα regulates DNMT1 to promote demethylation of metabolic genes.** In human umbilical vein
387 endothelial cells and mesenchymal stem cells cultured in vitro, AMPK phosphorylates DNMT1 to
388 promote transcription of metabolic genes, including *Ppargc1a* (17, 18). Hence, we hypothesized that
389 the lower expression of metabolic genes by tumor-infiltrating AMPKα1/α2-deficient Treg cells (see
390 Cluster 1 in Figure 2E-H) was a consequence of DNA hypermethylation at their gene promoters. We

391 tested this hypothesis by performing genome-wide DNA methylation profiling of *Prkaa1/2*$^{fl/fl}$*Foxp3*$^{YFP-}$
392 ^{Cre} and control Treg cells sorted from B16 melanoma tumors and from spleens at homeostasis. While
393 there was no difference in genome-wide promoter methylation, we observed hypermethylation of Clus-
394 ter 1 gene promoters in AMPKα1/α2-deficient tumor-infiltrating Treg cells, as well as hypermethylation
395 of *Ppargc1a* (PGC-1α) in tumor-infiltrating and splenic AMPKα1/α2-deficient Treg cells (Figure 6A-C).
396 While we found that AMPKα1/α2-deficient splenic Treg cells exhibited a trend (p = 0.067) toward higher
397 DNMT1 protein levels relative to controls, they had no differences in *Dnmt1* gene expression (Figure
398 6D-E). AMPKα1-deficient Treg cells exhibited similar, and AMPKα2-deficient Treg cells a trend toward
399 lower, DNMT1 protein expression relative to controls, respectively (Supplemental Figure 10A). Co-
400 immunoprecipitation assays in primary mouse iTreg cells, Jurkat cells, and the Treg cell-like MT-2 cell
401 line (43, 44) identified a physical interaction between AMPKα1 and DNMT1 (Figure 6F and
402 Supplemental Figure 10B-C). To determine whether AMPK is present in the nucleus where it can
403 interact with DNMT1, we performed immunofluorescence imaging in iTreg cells as well as Jurkat and
404 FOXP3+ MT-2 cells. Consistent with their physical interaction, our imaging studies identified AMPKα1
405 in the nucleus (Figure 6G and Supplemental Figure 10D-E). The subcellular compartmentalization of
406 AMPKα1 was unaffected by activation with 5-aminoimidazole-4-carboxamide ribonucleoside (AICAR)
407 in MT-2 cells (Supplemental Figure 10F). Finally, we established the functional relevance of these find-
408 ings by demonstrating that inhibition of DNMT activity with decitabine (DAC)—a clinically-used agent
409 we showed in published work promotes Treg cell function and is sufficient to induce DNA
410 hypomethylation in Treg cells (34)—increased MitoTracker DR staining (mitochondrial
411 mass/membrane potential) in AMPKα1/α2-sufficient splenic Treg cells in a dose-dependent manner
412 (Figure 6H). Treatment of AMPKα1/α2-deficient Treg cells with DAC also rescued MitoTracker DR
413 signal to that of untreated control Treg cells, confirming that DNA methylation regulates mitochondrial
414 mass in AMPKα1/α2-deficient Treg cells. Altogether, these experimental data reveal AMPK as a

415 nuclear factor that regulates DNMT1 in Treg cells to promote expression of metabolic factors that
416 potentiate mitochondrial metabolism.

417 **Discussion**

418

419 Treg cells exhibit metabolic plasticity in the TME, which in turn supports Treg cell suppressive function
420 (12, 13). Nevertheless, mechanisms that orchestrate the metabolic adaptation of tumor-infiltrating Treg
421 cells remain undetermined. Here, our experimental data revealed that AMPK-deficient Treg cells failed
422 to exert optimal suppressive function in metabolically stressed microenvironments. We found that
423 AMPK-deficient Treg cells were unable to augment their oxygen consumption under the stress of a
424 mitochondrial uncoupling agent ex vivo, failed to upregulate genes supporting mitochondrial
425 metabolism in the TME, and did not sustain proper mitochondrial mass/membrane potential or
426 metabolic homeostasis during viral pneumonia. These results credential AMPK as a key mediator of
427 Treg cell metabolic adaptation to settings of microenvironmental stress, likely through potentiation of
428 mitochondrial metabolism, and are consistent with in vitro experiments suggesting AMPK potentiates
429 Treg cell suppressive function (45).

430

431 While comparison of the metabolomic profiles of the TME and virus-injured lung interstitial fluid showed
432 similar alterations when compared with plasma, we observed differences in the abundance of a small
433 set of metabolites between these two interstitial fluid compartments, including glucose and glutamine,
434 which were lower in the TME compared with the lung during viral pneumonia. In most cell types,
435 increases in the AMP-to-ATP ratio from glucose deprivation and other states of energy stress lead to
436 phosphorylation of AMPK by liver kinase B1 (LKB1) (46). Notably, Treg cells require LKB1 to sustain
437 immune self-tolerance at homeostasis, albeit in an AMPK signaling-independent manner (19, 21). Cell
438 signaling events such as T cell receptor (TCR) engagement also activate AMPK via
439 calcium/calmodulin-dependent protein kinase kinase (CaMKK) (16, 47). These AMPK-activating events
440 likely contribute to the metabolic adaptation mediated by Treg cell AMPK in disease microenvironments
441 and serve as independent inputs through which AMPK can sense and respond to the extracellular

442 milieu. Therefore, it is plausible that the loss-of-function we observed in tumor-infiltrating AMPK-
443 deficient Treg cells is driven by an inability to adapt to glucose or other nutrient deprivation, whereas
444 lung Treg cells require AMPK during influenza to adapt to different metabolic and signaling challenges.
445 It remains unclear what dimensions of Treg cell function are lost in AMPK-deficient Treg cells in these
446 microenvironments, as our measurements of classical surface molecules via which Treg cells exert
447 their suppressive function did not reveal broad changes in Treg cell suppressive phenotype.
448 Nevertheless, we detected greater IFN-γ production in intra-tumoral CD8+ T cells in mice with Treg
449 cell-specific AMPK deficiency, indicating a loss of classical suppressive function.
450
451 Our experimental data suggest that AMPK regulates DNMT1 to activate the expression of metabolic
452 genes that support mitochondrial function, including *Ppargc1a*/PGC-1α. In some cell types cultured in
453 vitro, an AMPK-DNMT1-mitochondrial metabolism axis regulates metabolic function (17, 18). In vivo,
454 we found in tumor-infiltrating Treg cells that AMPK serves as an epigenetic regulator of transcriptional
455 programs that support metabolic function and the Treg cell lineage. Loss of AMPK in Treg cells led to
456 DNA hypermethylation at the promoters of key metabolic genes in the TME. Our co-
457 immunoprecipitation studies confirmed that AMPKα1 directly interacts with DNMT1, likely regulating
458 DNMT1 activity via phosphorylation events suggested by in vitro studies (17, 18). Critically, treatment
459 with the DNMT inhibitor decitabine rescued mitochondrial mass in AMPK-deficient Treg cells with a
460 dose-response correlation that was steeper in AMPK-sufficient compared with -deficient cells,
461 mechanistically connecting AMPK, DNMT1, and mitochondria. These findings are consistent with the
462 higher degree of DNA methylation present in AMPK-deficient cells, making them relatively more
463 resistant to the effect of DNA methyltransferase inhibition. Additional mechanisms may link AMPK to
464 DNA methylation writer complexes. For example, UHRF1, the non-redundant DNMT1 adapter protein
465 we previously showed to be necessary for Treg cell identity and function (23), has been reported to
466 inhibit AMPK function in the nucleus of hepatocytes (48). Hence, AMPK may regulate DNA methylation

467 in Treg cells via interaction with other DNMT complex members such as UHRF1. Finally, multifactorial
468 mechanisms induce and regulate FOXP3 expression in harsh settings such as the tumor
469 microenvironment (49-51). While we found a nominally lower level of FOXP3 protein expression in
470 AMPK-deficient compared with AMPK-sufficient Treg cells at baseline, this difference was not evident
471 in the tumor and infected lung microenvironments, indicating that the mechanisms controlling FOXP3
472 level in these settings are not dependent on AMPK. Interestingly, we observed lower *Foxp3* gene
473 expression by RNA-seq in AMPK-deficient Treg cells isolated from the TME at day 12 but not at day
474 15, suggesting important regulatory events occurring over the course of tumor growth.
475
476 The context-specific upregulation of *Prkaa2* in tumor-infiltrating Treg cells may explain the discrepant
477 consequences for anti-tumor immunity reported in Treg cell-specific AMPKα1-deficient mice challenged
478 with B16 melanoma tumors (29, 30). A study assessing the contribution of each AMPK catalytic subunit
479 isoform to the potentiation of mitochondrial gene expression found that AMPKα2, but not AMPKα1, is
480 required for the upregulation of *Ppargc1a* expression during myotube differentiation (52). While we
481 showed that AMPKα1 also interacts with DNMT1 in T cell lines and primary FOXP3^{+} T cells, it is
482 plausible that the two AMPKα isoforms exert differential regulation over epigenetic modifiers in the
483 TME. Therefore, *Prkaa2* upregulation by tumor-infiltrating, AMPKα1-deficient Treg cells may impact
484 Treg cell suppressive function and thereby lead to conflicting results, especially if *Prkaa2* upregulation
485 is modified by variables that are difficult to control across studies, such as the mouse colony microbiome
486 (53). Indeed, our data suggest that, while AMPKα1 and AMPKα2 may have a shared set of downstream
487 targets that are necessary for Treg cell function in the TME and the lung during viral pneumonia,
488 isoform-specific activities may have divergent influences on Treg cell function, as evidenced by the
489 dichotomous tumor burden relative to control mice observed in *Prkaa1*$^{fl/fl}$*Foxp3*$^{YFP\text{-}Cre}$ and
490 *Prkaa2*$^{fl/fl}$*Foxp3*$^{YFP\text{-}Cre}$ mice.
491

492 Clinical trial data suggest that metformin, an indirect AMPK activator, significantly reduces the risk of
493 developing long COVID (54-56). This finding is consistent with the observed effects of metformin on
494 mouse models of lung injury (57, 58). Our data support that AMPK is dispensable for Treg cell-mediated
495 immune self-tolerance yet promotes Treg cell suppressive function in disease microenvironments. This
496 context-specific requirement of AMPK for Treg cell function makes it an attractive drug target for
497 attempts to potentiate the function of Treg cells ex vivo before their use in cell-based therapies, such
498 as those being leveraged in early phase clinical trials to improve outcomes in patients with COVID-19
499 (59, 60).
500
501 Our study has limitations. First, AMPK phosphorylates specific residues of DNMT1 in human umbilical
502 vein endothelial cells to decrease DNMT1 activity (17). Unfortunately, antibodies specific for the
503 homologous residues of mouse DNMT1 are not available. Regardless, our co-immunoprecipitation,
504 immunofluorescence, immunoassay, and sequencing data support that AMPK regulates DNMT1 in
505 Treg cells. Second, we detected 159 metabolites via LC-MS in ~$5x10^4$ Treg cells sorted from the
506 influenza virus-injured lung at peak injury. While we were able to detect an accumulation of pyruvic acid
507 and lactic acid in AMPK-deficient Treg cells suggestive of an impaired TCA cycle, a more
508 comprehensive assessment of the Treg cell metabolome during viral pneumonia may have provided
509 insight into whether the loss-of-function in this context is due to energy stress in the absence of AMPK-
510 mediated metabolic adaptation. Finally, the loss of AMPK-dependent regulation of transcriptomic and
511 epigenetic signatures may be too complex to cause the resulting Treg cell loss-of-function via a single
512 factor, such as dampened *Ppargc1a* expression; the combined dysregulation of more than one
513 downstream target of AMPK is likely to mediate the loss of function.
514
515 In summary, our findings support a model in which AMPK coordinates the metabolic adaptation of Treg
516 cells in settings of microenvironmental stress by potentiating mitochondrial metabolism, consistent with

517 AMPK's canonical function as a sensor of energetic stress and the central role mitochondrial
518 metabolism plays in programming Treg cell functional state. We show that this AMPK-mediated
519 metabolic adaptation is executed in part through the regulation of DNA methylation at key metabolic
520 loci, offering potential pharmacologic targets to modulate Treg cell function in disease, including in
521 severe lung injury and cancer.

522 **Methods**

523

524 **Sex as a biological variable.** Sex was not considered as a biological variable in all experiments. See
525 **Supplemental Methods** for further details.

526

527 **Mice**. *Prkaa1*$^{fl/fl}$ (cat. no. 014141), *Prkaa2*$^{fl/fl}$ (cat. no. 014142), and *Foxp3*$^{YFP\text{-}Cre}$ (cat. no. 016959) mice
528 from the C57BL/6J genetic background were purchased from The Jackson Laboratory. All animals were
529 genotyped using services provided by Transnetyx Inc., with primers provided by The Jackson
530 Laboratory and shown in **Supplemental Table 1**. Animals received water *ad libitum*, were housed at a
531 temperature range of 20 °C–23 °C under 14-hour light/10-hour dark cycles and received standard
532 rodent chow. See **Supplemental Methods** for further details.

533

534 **Flow cytometry and cell sorting**. Single-cell suspensions of organ tissues, blood, tumors, or cultured
535 cells were prepared and stained for flow cytometry analysis and sorting as previously described (23,
536 35) using the reagents shown in **Supplemental Table 2**. See **Supplemental Methods** for further
537 details.

538

539 **Imaging flow cytometry measurement of mitophagy**. Splenic single cell suspensions were stained
540 with surface markers and MitoView Green (20 nM) and treated with 10 μM CCCP for 30, 60, 120, and
541 180 minutes to induce mitophagy. Samples were then fixed as above. Fixed single cell suspensions
542 were then stained with anti-LAMP1 and anti-FOXP3 antibodies at 4°C for 30 minutes. Imaging flow
543 cytometry was performed using a BD FACS Discover S8 cell sorter and analyzer and the subcellular
544 co-localization of LAMP1 and MitoView Green signal was assessed using BD CellView Image
545 Technology in the BD FACSChorus software.

546

547 **iTreg cell induction and culture.** iTreg cells were induced and cultured as previously described (23).
548 See **Supplemental Methods** for further details.
549
550 **B16 melanoma tumor model**. B16-F10 cells (ATCC CRL-6475) were cultured as previously described
551 (23). 250,000 B16-F10 cells were resuspended in 0.1 mL of PBS and 40% Matrigel (Corning cat. #
552 356237) and injected subcutaneously in the hair-trimmed flanks of 12–15-week-old mice. See
553 **Supplemental Methods** for further details.
554
555 **Influenza A virus administration**. Mice were anesthetized with isoflurane and intubated using a 20-
556 gauge angiocatheter cut to a length that placed the tip of the catheter above the carina. Mice were
557 instilled with mouse-adapted influenza A/WSN/33 [H1N1] virus (12.5 plaque-forming units in 50 μL of
558 sterile PBS) as previously described (35).
559
560 **Measurement of physiologic readouts of influenza pneumonia progression and resolution.**
561 Arterial blood oxygen saturation (SpO_2) was measured in control and influenza virus-infected mice
562 using a MouseOx Plus pulse oximeter (Starr Life Sciences). Beginning on the fifth day post-inoculation
563 and continuing every other, SpO_2 was measured with oximeter collar clips secured to the hairless neck
564 of conscious, immobilized animals. Mouse weights were recorded the day of influenza virus inoculation
565 and every other day post-inoculation starting day 5. Mouse weights were normalized to those recorded
566 on the day of inoculation.
567
568 **Lung tissue harvesting and processing**. These procedures have been previously reported (35). See
569 **Supplemental Methods** for further details.
570

571 **Immunoblotting.** Cultured cells were lysed for one hour at 4°C in lysis buffer (Cell Signaling cat. no.
572 9803) supplemented with phosphatase (Cell Signaling cat. no. 5870S) and protease inhibitors (Roche,
573 cat. no. 65726900) after which their concentration was measured with a BCA assay according to
574 manufacturer instructions (Pierce cat. no. 23225). Cell lysates were subjected to gel electrophoresis
575 and transferred to membranes that were incubated with an antibody against AMPKα1 (Abcam cat. no.
576 ab32047), DNMT1 (Cell Signaling cat. no. 5032) and β-actin (Abcam cat. no. ab8227) overnight at 4
577 °C with constant agitation.
578
579 **Wes protein immunoassay.** Flow cytometry-sorted cells were lysed, and the resulting lysate protein
580 concentrations were measured as described above. For protein measurements using the Simple Wes
581 immunoassay system, 0.5 µg of protein in 3 µL were loaded per well and processed according to
582 manufacturing instructions. The following concentrations were used for primary antibodies: 1:50 anti-
583 DNMT1 (Invitrogen cat. no. MA5-16169), 1:50 anti-AMPKα (Cell Signaling cat. no. 2532S), and 1:50
584 anti-β-actin (Abcam cat. no. ab8227).
585
586 **Co-immunoprecipitation assay.** 10^6 cells were lysed in cell lysis buffer for one hour at 4 °C as
587 described above. Lysates were incubated with an antibody against AMPKα1 (Abcam cat. no. ab32047)
588 or isotype control (Cell Signaling cat. no. 7074) overnight at 4 °C with constant agitation. The immune
589 complex was precipitated with Dyna Protein G beads (Life Technologies cat. no. 10003D), washed and
590 resuspended in SDS/PAGE loading buffer, and heated to 95 °C for 5 minutes. Processed samples were
591 then blotted with antibodies against DNMT1 (Cell Signaling cat. no. 5032), AMPKα1 (Abcam cat. no.
592 ab32047), and β-actin (Abcam cat. no. ab8227). Jurkat cells were obtained from ATCC. MT-2 cells
593 were a gift from Jason R. Mock, MD, PhD (University of North Carolina, Chapel Hill, NC).
594

595 **Immunofluorescence for microscopy.** 10^6 cells were fixed with ice-cold 100% methanol for 5
596 minutes. Subsequently, samples were processed with Immunofluorescence Application Solutions Kit
597 (Cell Signaling cat. no. 12727) following the manufacturer's protocol. Cells were stained overnight at 4
598 °C with anti-DNMT1 (Abcam cat. no. ab21799 1), anti-AMPKα1 (Abcam cat. no. ab32047), Alexa fluor
599 488-conjugated isotype control (Abcam cat. no. ab199091), or unconjugated isotype control (Abcam
600 cat. no. ab172730). The following day, cells that were stained with anti-AMPKα1 antibody and
601 unconjugated isotype control antibody were incubated in the dark at room temperature for 2 hours with
602 anti-rabbit Alexa Fluor 488 secondary antibody (Abcam cat. no. ab150113). Following antibody
603 incubation, cells were mounted on a slide with VECTASHIELD Vibrance mounting medium containing
604 DAPI (Vector Labs cat. no. H-1800). Fluorescent images were acquired at room temperature using a
605 confocal microscope (Nikon) with 40× magnification at the Northwestern Center for Advanced
606 Microscopy.
607
608 **Nuclear-cytoplasmic fractionation assay.** $5x10^6$ MT-2 cells were treated and subsequently
609 underwent lysis using NE-PER™ Nuclear and Cytoplasmic Extraction kit (ThermoFisher cat. no. 78833)
610 according to manufacturer's protocol. Nuclear and cytoplasmic fractions were collected and further
611 analyzed for the expression of proteins of interest with immunoblotting as described above.
612
613 **Metabolic flux (Seahorse) assay.** $2.5x10^5$ flow cytometry-sorted Treg cells were seeded on a 96-well
614 Seahorse cell culture plate and analyzed on a Seahorse XF24 Analyzer (10). The following drugs and
615 corresponding doses were loaded onto ports A, B, C, and D in the same order: oligomycin (2.5 μM,
616 Sigma-Aldrich cat no. 75351), CCCP (10 μM, Sigma-Aldrich cat no. C2759), antimycin A/piercidin (2
617 μM each, Sigma-Aldrich cat no. A8674 and 15379, respectively), and 2-deoxyglucose (25 mM, Sigma-
618 Aldrich cat no. D8375).
619

620 **RNA-sequencing, modified reduced representation bisulfite sequencing (mRRBS) and analysis.**
621 Nucleic acid isolation and next-generation sequencing library preparation was performed using custom
622 procedures previously described by our group (23, 35, 61). RNA-seq and mRRBS analysis was
623 performed using previously published procedures (62). See **Supplemental Methods** for further details.
624
625 **Collection of lung Treg cells for metabolomics**. Lung single-cell suspensions were subjected to
626 CD4+ cell positive enrichment according to kit manufacturer's instructions (Miltenyi Biotec cat. no. 130-
627 097-048) before fluorochrome staining. Using a MACSQuant Tyto, 5-10x10^5 lung Treg cells were sorted
628 from each pair of lungs. Sorted cells were centrifuged at 500 rcf for 6 minutes, 4 °C. Pelleted cells were
629 resuspended in 15 µl of 80% acetonitrile and vortexed for 30 seconds. Following centrifugation for 30
630 min at 20,000 rcf, 4 °C, the supernatant was collected LC-MS. See **Supplemental Methods** for further
631 details.
632
633 **Collection of interstitial fluid and plasma for metabolomics.** Blood was centrifuged at 800 rcf for
634 10 minutes at 4 °C in EDTA tubes. The plasma phase was pipetted, frozen with liquid nitrogen, and
635 stored at -80 °C. Intact tumors and lungs were centrifuged at 100 rcf for 10 minutes at 4 °C in centrifuge
636 tubes containing a 0.22 µm filter (Costar cat. no. 8160). The extracted interstitial fluid was then diluted
637 1 to 5 in 80% acetonitrile and vortexed for 30 seconds. The diluted interstitial fluid was centrifuged for
638 30 min at 20,000 rcf at 4 °C and the supernatant was collected for LC-MS analysis. See **Supplemental**
639 **Methods** for further details.
640
641 **High-performance liquid chromatography and high-resolution mass spectrometry and tandem**
642 **mass spectrometry (LC-MS) for metabolomics.** The system consisted of a Thermo Q-Exactive in
643 line with an electrospray source and an Ultimate3000 (Thermo) series HPLC consisting of a binary
644 pump, degasser, and auto-sampler outfitted with a Xbridge Amide column (Waters; dimensions of 3.0

645 mm × 100 mm and a 3.5 μm particle size). Data acquisition and analysis were carried out by Xcalibur
646 4.1 software and Tracefinder 4.1 software, respectively (both from Thermo Fisher Scientific). See
647 **Supplemental Methods** for further details.
648
649 **LC-MS data analysis.** Raw peak intensity data of the metabolites detected by LC-MS were uploaded
650 to Metaboanalyst 5.0's statistical analysis [one factor] module. For comparisons with more than two
651 groups, one-way ANOVA with $q < 0.05$ was employed to identify significant differentially enriched
652 metabolites. Comparisons with only two groups were analyzed with multiple parametric t-tests and fold-
653 change analysis using Metabonalyst 5.0's standard settings ($p < 0.1$). Fold change threshold was set
654 to 1.5 in resulting volcano plots to increase the power of the downstream overrepresentation analysis.
655 See **Supplemental Methods** for further details.
656
657 **Statistical analysis.** *p*-values and FDR *q*-values resulting from two-tailed tests were calculated using
658 statistical tests stated in the figure legends using GraphPad Prism v10.1.0. Differences between groups
659 with *p* or *q* values < 0.05 were considered statistically significant; see LC-MS data analysis for the
660 statistical approach to metabolomic profiling data and RNA-sequencing, modified reduced
661 representation bisulfite sequencing (mRRBS) and analysis for the statistical approach to transcriptomic
662 and epigenomic profiling data. Using the ROUT method, the following number of outliers were excluded
663 from the following figures: one from Figure 2B (Q = 0.5%) two from Figure 2C (Q = 0.5%), four from
664 Supplemental Figure 2L (Q = 1.0%) and three from Supplemental Figure 4B (Q = 1.0%). Central
665 tendency and error are displayed as mean ± standard deviation (SD) except as noted. Box plots show
666 median and quartiles. Numbers of biological replicates are stated in the figures or accompanying
667 legends.
668

669 **Study approval.** All mouse procedures were approved by the Northwestern University IACUC under
670 protocols IS00012519 and IS00017837.
671
672 **Data availability.** The raw and processed next-generation sequencing data sets were deposited in the
673 NCBI's Gene Expression Omnibus database (GEO GSE249019). Raw peak intensity data of annotated
674 metabolites detected by LC-MS are available in the data supplement. All raw data is included in the
675 Supporting Data Values file.
676
677

678 **Author contributions.** MATA contributed to the conceptualization and methodology of this work; the
679 data generation and visualization; the funding acquisition for this work; and to the writing and editing of
680 the manuscript. JKG contributed to the generation of data and the editing of the manuscript. QL
681 contributed to the methodology, generation and visualization of data, and the editing of the manuscript.
682 NM contributed to the methodology, generation and visualization of data, and the editing of the
683 manuscript. CPRF contributed to the methodology, generation of data, and the editing of the
684 manuscript. KAH contributed to the methodology, generation of data, and the editing of the manuscript.
685 AMJ contributed to the generation of data and the editing of the manuscript. LM-N contributed to the
686 methodology, generation of data, and the editing of the manuscript. KC contributed to the generation
687 of data and the editing of the manuscript. HA-V contributed to the methodology, generation of data, and
688 the editing of the manuscript. SEW contributed to the conceptualization and methodology of this work;
689 the data generation and visualization; the supervision of this work; and to the writing and editing of the
690 manuscript. BDS contributed to the conceptualization and methodology of this work; the data
691 generation and visualization; the supervision, administration, and funding acquisition of this work; and
692 to the writing and editing of the manuscript.
693

694 **Acknowledgements.** MATA is supported by NIH awards T32GM144295, T32HL076139, and
695 F31HL162490. JKG is supported by NIH awards T32GM144295 and T32HL076139. QL is supported
696 by the David W. Cugell Fellowship and The Genomics Network (GeNe) Pilot Project Funding. NM is
697 supported by NIH award T32AI083216. CPRF is supported by T32HL076139. AMJ is supported by NIH
698 award F32HL162418. LM-N is supported by the NIH awards K08HL159356, U19AI135964 and the
699 Parker B. Francis Opportunity Award. KC is supported by NIH award T32GM144295. SEW is supported
700 by the Burroughs Wellcome Fund Career Awards for Medical Scientists. BDS is supported by NIH
701 awards R01HL149883, R01HL153122, P01HL154998, P01AG049665, U19AI135964, and
702 U19AI181102. We wish to acknowledge the Northwestern University Flow Cytometry Core Facility

supported by CA060553; the BD FACSAria SORP system was purchased with the support of S10OD011996. We also wish to acknowledge the Northwestern University RNA-Seq Center/Genomics Lab of the Pulmonary and Critical Care Medicine and Rheumatology Divisions. Histology services were provided by the Northwestern University Mouse Histology and Phenotyping Laboratory, which is supported by P30CA060553 awarded to the Robert H. Lurie Comprehensive Cancer Center. This research was supported in part through the computational resources and staff contributions provided by the Genomics Compute Cluster, which is jointly supported by the Feinberg School of Medicine, the Center for Genetic Medicine, and Feinberg's Department of Biochemistry and Molecular Genetics, the Office of the Provost, the Office for Research, and Northwestern Information Technology. The Genomics Compute Cluster is part of Quest, Northwestern University's high performance computing facility, with the purpose to advance research in genomics. The graphical abstract was created using BioRender.com under an academic license.

717 **References**

718 1. Sakaguchi S, Sakaguchi N, Asano M, Itoh M, Toda M. Immunologic self-tolerance maintained
719 by activated T cells expressing IL-2 receptor alpha-chains (CD25). Breakdown of a single
720 mechanism of self-tolerance causes various autoimmune diseases. *J Immunol.* 1995;155:1151-
721 1164.

722 2. Bacchetta R, et al. Defective regulatory and effector T cell functions in patients with FOXP3
723 mutations. *J Clin Invest.* 2006;116(6):1713-1722.

724 3. Weinberg SE, Singer BD. Toward a paradigm to distinguish distinct functions of FOXP3(+)
725 regulatory T cells. *Immunohorizons.* 2021;5(12):944-952.

726 4. Fisher SA, et al. Transient Treg depletion enhances therapeutic anti-cancer vaccination. *Immun*
727 *Inflamm Dis.* 2017;5(1):16-28.

728 5. Stewart CA, et al. Interferon-dependent IL-10 production by Tregs limits tumor Th17
729 inflammation. *J Clin Invest.* 2013;123(11):4859-4874.

730 6. Jovisic M, Mambetsariev N, Singer BD, Morales-Nebreda L. Differential roles of regulatory T
731 cells in acute respiratory infections. *Journal of Clinical Investigation.* 2023;133(14).

732 7. Arpaia N, et al. A distinct function of regulatory T cells in tissue protection. *Cell.*
733 2015;162(5):1078-1089.

734 8. Cluxton D, Petrasca A, Moran B, Fletcher JM. Differential regulation of human Treg and Th17
735 cells by fatty acid synthesis and glycolysis. *Front Immunol.* 2019;10:115.

736 9. Beier UH, et al. Essential role of mitochondrial energy metabolism in Foxp3(+) T-regulatory cell
737 function and allograft survival. *FASEB J.* 2015;29(6):2315-2326.

738 10. Weinberg SE, et al. Mitochondrial complex III is essential for suppressive function of regulatory
739 T cells. *Nature.* 2019;565(7740):495-499.

740 11. Angelin A, et al. Foxp3 reprograms T cell metabolism to function in low-glucose, high-lactate
741 environments. *Cell Metab.* 2017;25(6):1282-1293 e1287.

742 12. Wang H, et al. CD36-mediated metabolic adaptation supports regulatory T cell survival and
743 function in tumors. *Nat Immunol.* 2020;21(3):298-308.
744 13. Watson MJ, et al. Metabolic support of tumour-infiltrating regulatory T cells by lactic acid. *Nature.*
745 2021;591(7851):645-651.
746 14. Herzig S, Shaw RJ. AMPK: Guardian of metabolism and mitochondrial homeostasis. *Nat Rev*
747 *Mol Cell Biol.* 2018;19(2):121-135.
748 15. Yan Y, Zhou XE, Xu HE, Melcher K. Structure and physiological regulation of AMPK. *Int J Mol*
749 *Sci.* 2018;19(11).
750 16. Willows R, et al. Phosphorylation of AMPK by upstream kinases is required for activity in
751 mammalian cells. *Biochem J.* 2017;474(17):3059-3073.
752 17. Marin TL, et al. AMPK promotes mitochondrial biogenesis and function by phosphorylating the
753 epigenetic factors DNMT1, RBBP7, and HAT1. *Sci Signal.* 2017;10(464).
754 18. Wu J, Gulati S, Teague AM, Kim Y, Tryggestad JB, Jiang S. AMPK regulates DNA methylation
755 of PGC-1alpha and myogenic differentiation in human mesenchymal stem cells. *Stem Cells Dev.*
756 2023;32(5-6):131-139.
757 19. Yang K, et al. Homeostatic control of metabolic and functional fitness of Treg cells by lkb1
758 signalling. *Nature.* 2017;548(7669):602-606.
759 20. He N, et al. Metabolic control of regulatory T cell (Treg) survival and function by lkb1. *Proc Natl*
760 *Acad Sci U S A.* 2017;114(47):12542-12547.
761 21. Timilshina M, et al. Activation of mevalonate pathway via lkb1 is essential for stability of Treg
762 cells. *Cell Rep.* 2019;27(10):2948-2961 e2947.
763 22. Wu D, et al. Lkb1 maintains Treg cell lineage identity. *Nat Commun.* 2017;8:15876.
764 23. Helmin KA, et al. Maintenance DNA methylation is essential for regulatory T cell development
765 and stability of suppressive function. *J Clin Invest.* 2020;130(12):6571-6587.

766 24. Gualdoni GA, Mayer KA, Goschl L, Boucheron N, Ellmeier W, Zlabinger GJ. The AMP analog
767 aicar modulates the Treg/Th17 axis through enhancement of fatty acid oxidation. *FASEB J.*
768 2016;30(11):3800-3809.
769 25. Duan W, et al. Metformin mitigates autoimmune insulitis by inhibiting Th1 and Th17 responses
770 while promoting Treg production. *Am J Transl Res.* 2019;11(4):2393-2402.
771 26. Miyara M, et al. Functional delineation and differentiation dynamics of human CD4+ T cells
772 expressing the FoxP3 transcription factor. *Immunity.* 2009;30(6):899-911.
773 27. Santagata S, et al. Targeting cxcr4 reverts the suppressive activity of T-regulatory cells in renal
774 cancer. *Oncotarget.* 2017;8(44):77110-77120.
775 28. Kidani Y, et al. CCR8-targeted specific depletion of clonally expanded Treg cells in tumor tissues
776 evokes potent tumor immunity with long-lasting memory. *Proc Natl Acad Sci U S A.* 2022;119(7).
777 29. Pokhrel RH, et al. AMPK promotes antitumor immunity by downregulating PD-1 in regulatory T
778 cells via the HMGCR/p38 signaling pathway. *Mol Cancer.* 2021;20(1):133.
779 30. An J, et al. AMP-activated protein kinase alpha1 promotes tumor development via FOXP3
780 elevation in tumor-infiltrating Treg cells. *iScience.* 2022;25(1):103570.
781 31. Singer BD, Chandel NS. Immunometabolism of pro-repair cells. *J Clin Invest.* 2019;129(7):2597-
782 2607.
783 32. Jovisic M, Mambetsariev N, Singer BD, Morales-Nebreda L. Differential roles of regulatory T
784 cells in acute respiratory infections. *J Clin Invest.* 2023;133(14).
785 33. D'Alessio FR, et al. CD4+CD25+Foxp3+ Tregs resolve experimental lung injury in mice and are
786 present in humans with acute lung injury. *J Clin Invest.* 2009;119(10):2898-2913.
787 34. Singer BD, et al. Regulatory T cell DNA methyltransferase inhibition accelerates resolution of
788 lung inflammation. *Am J Respir Cell Mol Biol.* 2015;52(5):641-652.
789 35. Morales-Nebreda L, et al. Aging imparts cell-autonomous dysfunction to regulatory T cells during
790 recovery from influenza pneumonia. *JCI Insight.* 2021;6(6).

791 36. Gao CA, et al. Machine learning links unresolving secondary pneumonia to mortality in patients
792 with severe pneumonia, including COVID-19. *J Clin Invest.* 2023;133(12).
793 37. Blagih J, et al. The energy sensor AMPK regulates T cell metabolic adaptation and effector
794 responses in vivo. *Immunity.* 2015;42(1):41-54.
795 38. Shaw M, Palese P. *Orthomyxoviridae: The viruses and their replication in fields virology.*
796 Philadelphia: Lippencott Williams and Wilkins; 2006.
797 39. Kjobsted R, et al. AMPK and tbc1d1 regulate muscle glucose uptake after, but not during,
798 exercise and contraction. *Diabetes.* 2019;68(7):1427-1440.
799 40. Jang M, et al. AMPK contributes to autophagosome maturation and lysosomal fusion. *Sci Rep.*
800 2018;8(1):12637.
801 41. Inoki K, Zhu T, Guan KL. Tsc2 mediates cellular energy response to control cell growth and
802 survival. *Cell.* 2003;115(5):577-590.
803 42. Narendra D, Tanaka A, Suen DF, Youle RJ. Parkin is recruited selectively to impaired
804 mitochondria and promotes their autophagy. *J Cell Biol.* 2008;183(5):795-803.
805 43. Hamano R, Wu X, Wang Y, Oppenheim JJ, Chen X. Characterization of MT-2 cells as a human
806 regulatory T cell-like cell line. *Cell Mol Immunol.* 2015;12(6):780-782.
807 44. McCullough MJ, et al. Characterization of the MT-2 Treg-like cell line in the presence and
808 absence of forkhead box p3 (FOXP3). *Immunol Cell Biol.* 2024;102(3):211-224.
809 45. Braverman EL, et al. Overexpression of ampkgamma2 increases AMPK signaling to augment
810 human T cell metabolism and function. *J Biol Chem.* 2023;10.1016/j.jbc.2023.105488.105488.
811 46. Shaw RJ, et al. The tumor suppressor lkb1 kinase directly activates AMP-activated kinase and
812 regulates apoptosis in response to energy stress. *Proc Natl Acad Sci U S A.* 2004;101(10):3329-
813 3335.
814 47. Tamas P, et al. Regulation of the energy sensor AMP-activated protein kinase by antigen
815 receptor and ca2+ in T lymphocytes. *J Exp Med.* 2006;203(7):1665-1670.

816 48. Xu X, et al. Nuclear UHRF1 is a gate-keeper of cellular AMPK activity and function. *Cell Res.*
817 2021;10.1038/s41422-021-00565-y.
818 49. Montauti E, et al. A deubiquitination module essential for T(reg) fitness in the tumor
819 microenvironment. *Sci Adv.* 2022;8(47):eabo4116.
820 50. Cortez JT, et al. CRISPR screen in regulatory T cells reveals modulators of Foxp3. *Nature.*
821 2020;582(7812):416-420.
822 51. Joudi AM, Reyes Flores CP, Singer BD. Epigenetic control of regulatory T cell stability and
823 function: Implications for translation. *Front Immunol.* 2022;13:861607.
824 52. Okamoto S, Asgar NF, Yokota S, Saito K, Minokoshi Y. Role of the alpha2 subunit of AMP-
825 activated protein kinase and its nuclear localization in mitochondria and energy metabolism-
826 related gene expressions in c2c12 cells. *Metabolism.* 2019;90:52-68.
827 53. Smith PM, et al. The microbial metabolites, short-chain fatty acids, regulate colonic Treg cell
828 homeostasis. *Science.* 2013;341(6145):569-573.
829 54. Bramante CT, et al. Outpatient treatment of COVID-19 and incidence of post-COVID-19
830 condition over 10 months (COVID-OUT): A multicentre, randomised, quadruple-blind, parallel-
831 group, phase 3 trial. *Lancet Infect Dis.* 2023;10.1016/S1473-3099(23)00299-2.
832 55. Hawley SA, Gadalla AE, Olsen GS, Hardie DG. The antidiabetic drug metformin activates the
833 AMP-activated protein kinase cascade via an adenine nucleotide-independent mechanism.
834 *Diabetes.* 2002;51(8):2420-2425.
835 56. Meng S, et al. Metformin activates AMP-activated protein kinase by promoting formation of the
836 alphabetagamma heterotrimeric complex. *J Biol Chem.* 2015;290(6):3793-3802.
837 57. Guo Y, et al. Metformin alleviates allergic airway inflammation and increases Treg cells in obese
838 asthma. *J Cell Mol Med.* 2021;25(4):2279-2284.
839 58. Alwarawrah Y, et al. Targeting T-cell oxidative metabolism to improve influenza survival in a
840 mouse model of obesity. *Int J Obes (Lond).* 2020;44(12):2419-2429.

841 59. Gladstone DE, Kim BS, Mooney K, Karaba AH, D'Alessio FR. Regulatory T cells for treating
842 patients with COVID-19 and acute respiratory distress syndrome: Two case reports. *Ann Intern*
843 *Med.* 2020;173(10):852-853.
844 60. Gladstone DE, et al. Randomized, double-blinded, placebo-controlled trial of allogeneic cord
845 blood T-regulatory cells for treatment of COVID-19 ARDS. *Blood Adv.* 2023;7(13):3075-3079.
846 61. McGrath-Morrow SA, et al. DNA methylation regulates the neonatal CD4(+) T-cell response to
847 pneumonia in mice. *J Biol Chem.* 2018;293(30):11772-11783.
848 62. Singer BD. A practical guide to the measurement and analysis of DNA methylation. *Am J Respir*
849 *Cell Mol Biol.* 2019;61(4):417-428.
850
851

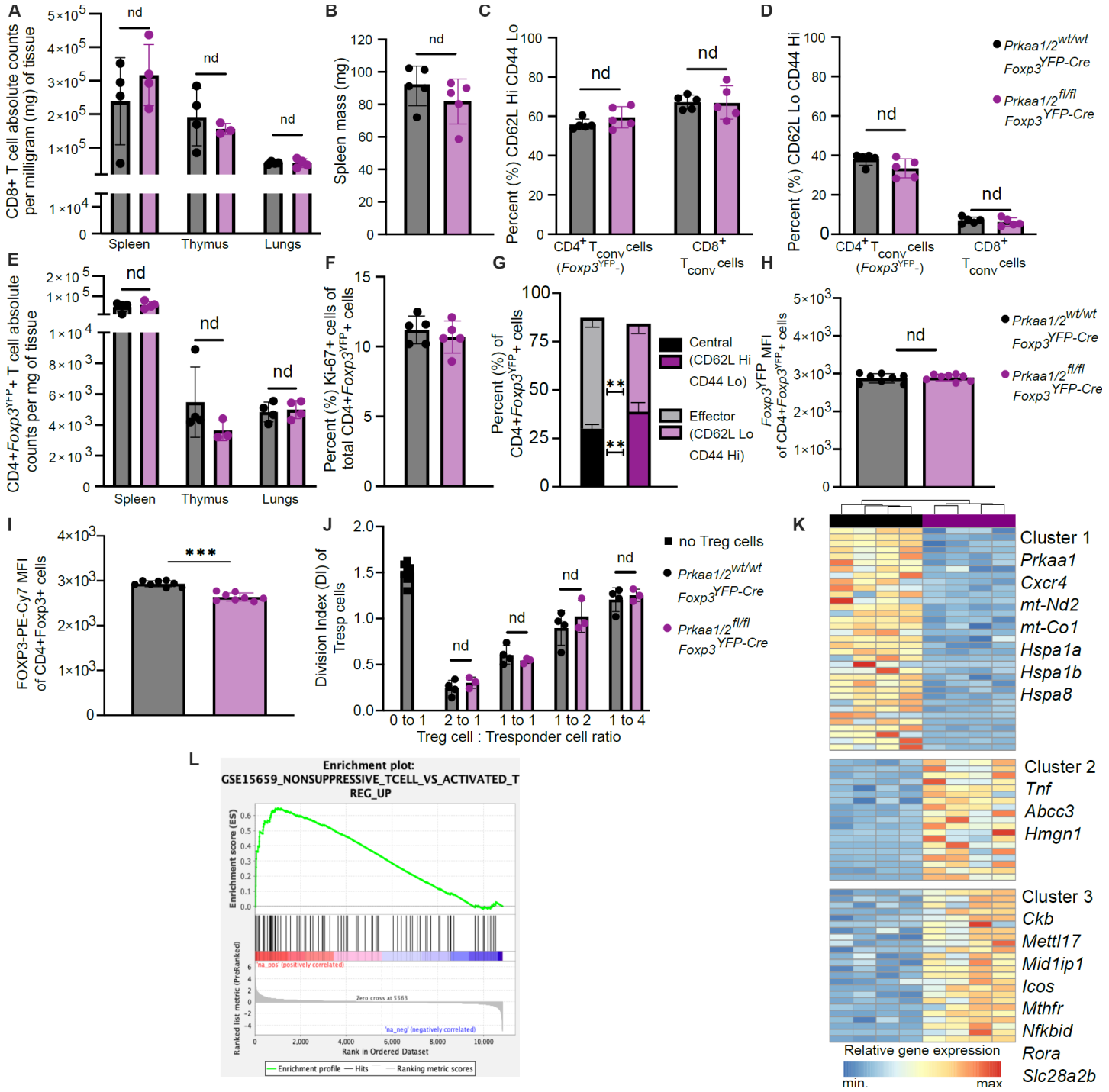

Figure 1. AMPKα1/α2 are dispensable for Treg cell-mediated immune self-tolerance and Treg cell suppressive function at homeostasis. (**A**) CD8+ conventional T (Tconv) cell absolute counts per milligram (mg) of *Prkaa1/2*$^{wt/wt}$*Foxp3*$^{YFP\text{-}Cre}$ (control) and *Prkaa1/2*$^{fl/fl}$*Foxp3*$^{YFP\text{-}Cre}$ mouse spleen (*n*=4 control, *n*=4 *Prkaa1/2*$^{fl/fl}$*Foxp3*$^{YFP\text{-}Cre}$), thymus (*n*=4 control, *n*=3 *Prkaa1/2*$^{fl/fl}$*Foxp3*$^{YFP\text{-}Cre}$), and lung (*n*=4 control, *n*=4 *Prkaa1/2*$^{fl/fl}$*Foxp3*$^{YFP\text{-}Cre}$). (**B**) Spleen mass of 8–12-week-old control (*n*=5) and *Prkaa1/2*$^{fl/fl}$*Foxp3*$^{YFP\text{-}Cre}$ (*n*=5) mice. (**C-D**) Frequency of naive (CD62L^{Hi}CD44^{Lo}; C) and effector (CD62^{Lo}CD44^{Hi}; D) splenic CD8+ and CD4+ Tconv cells out of total CD8+ and CD4+ cells, respectively (*n*=5 control, *n*=5 *Prkaa1/2*$^{fl/fl}$*Foxp3*$^{YFP\text{-}Cre}$). (**E**) CD4+*Foxp3*^{YFP}+ cell absolute counts per mg of control and *Prkaa1/2*$^{fl/fl}$*Foxp3*$^{YFP\text{-}Cre}$ mouse spleen (*n*=4 control, *n*=4 *Prkaa1/2*$^{fl/fl}$*Foxp3*$^{YFP\text{-}Cre}$), thymus (*n*=4 control, *n*=3 *Prkaa1/2*$^{fl/fl}$*Foxp3*$^{YFP\text{-}Cre}$), and lung (*n*=4 control, *n*=4 *Prkaa1/2*$^{fl/fl}$*Foxp3*$^{YFP\text{-}Cre}$). (**F**)

863 Frequency of Ki-67+CD4+*Foxp3*^{YFP}+ cells out of total CD4+*Foxp3*^{YFP}+ splenocytes (*n*=5 control, *n*=5
864 *Prkaa1/2*$^{fl/fl}$*Foxp3*$^{YFP\text{-}Cre}$). (**G**) Frequency of central (CD62L^{Hi}CD44^{Lo}) and effector (CD62^{Lo}CD44^{Hi})
865 CD4+*Foxp3*^{YFP}+ cells of total CD4+*Foxp3*^{YFP}+ splenocytes (*n*=5 control, *n*=5 *Prkaa1/2*$^{fl/fl}$*Foxp3*$^{YFP\text{-}Cre}$).
866 (**H-I**) *Foxp3*^{YFP} (H) and FOXP3-PE-Cy7 (I) mean fluorescence intensity (MFI) of CD4+*Foxp3*^{YFP}+
867 splenocytes (*n*=8 control, *n*=8 *Prkaa1/2*$^{fl/fl}$*Foxp3*$^{YFP\text{-}Cre}$). (**J**) Division index of CD4+*Foxp3*^{YFP}- splenic
868 responder T (Tresp) cells co-cultured with CD4+*Foxp3*^{YFP}+ splenocytes (*n*=4 control, *n*=3
869 *Prkaa1/2*$^{fl/fl}$*Foxp3*$^{YFP\text{-}Cre}$) for 72 hours. (**K**) *K*-means clustering of 78 significant differentially expressed
870 genes (FDR $q < 0.05$) identified between splenic CD4+*Foxp3*^{YFP}+ cells sorted from control (*n*=4) and
871 *Prkaa1/2*$^{fl/fl}$*Foxp3*$^{YFP\text{-}Cre}$ (*n*=4) mice with *k*=3 and scaled as *Z*-scores across rows. (**L**) Enrichment plot
872 of the GSE15659_NONSUPPRESSIVE_TCELL_VS_ACTIVATED_TREG_UP gene set generated
873 through gene set enrichment analysis (GSEA) preranked testing of the expressed genes of
874 *Prkaa1/2*$^{fl/fl}$*Foxp3*$^{YFP\text{-}Cre}$ and control splenic Treg cells identified by RNA-sequencing. ** *p* or *q* < 0.01;
875 *** *p* or *q* < 0.001; nd, no discovery, ns, not significant according to Mann-Whitney *U* test (B, F, H, I)
876 with two-stage linear step-up procedure of Benjamini, Krieger, and Yekutieli with Q = 5% (A, C, D, E,
877 G, J).
878

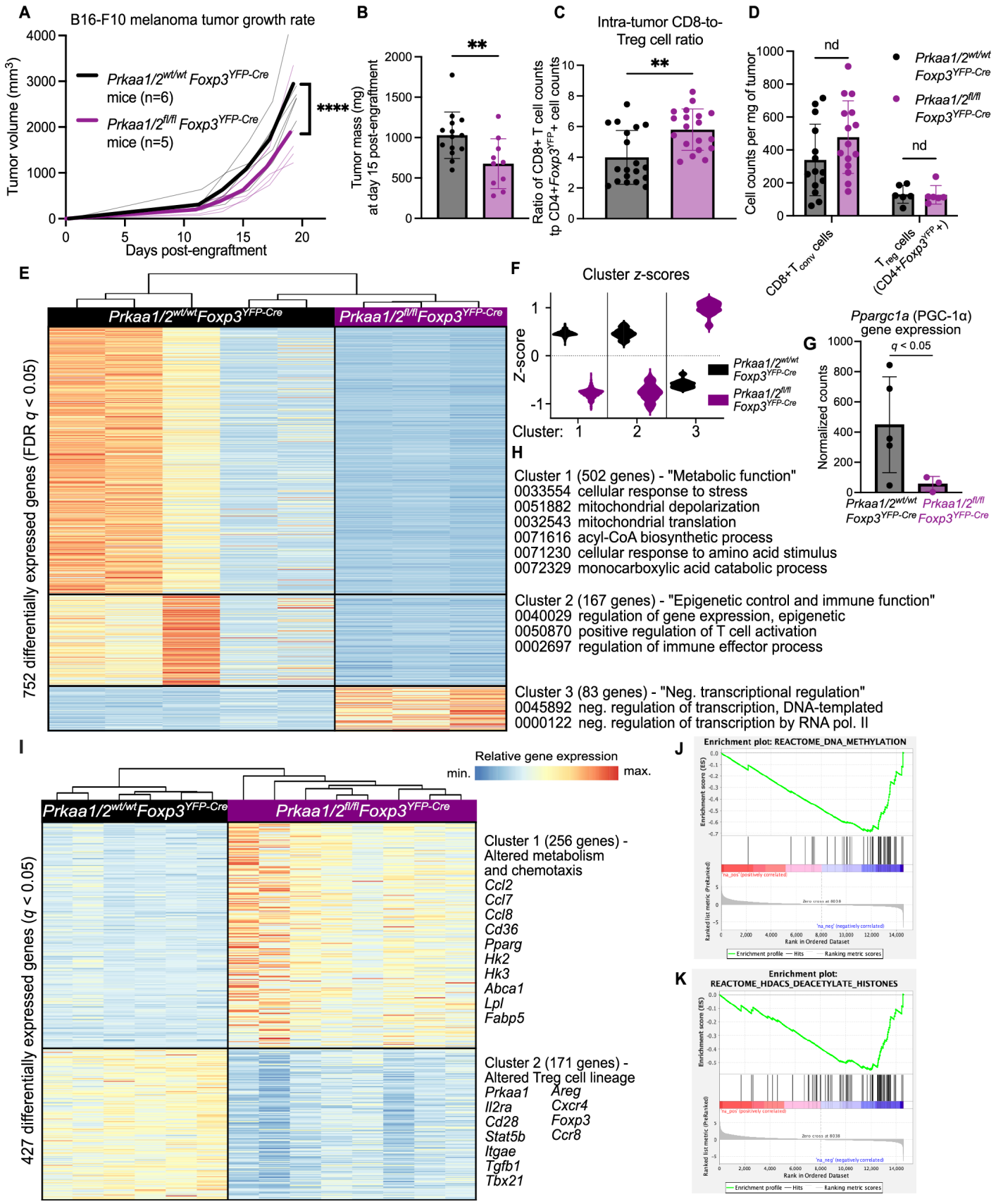

Figure 2. AMPKα1/α2 loss is sufficient to impair Treg cell suppressive function in the tumor microenvironment. (**A**) Growth of B16 melanoma tumors in *Prkaa1/2*$^{wt/wt}$*Foxp3*$^{YFP\text{-}Cre}$ (control, *n*=6)

882 and *Prkaa1/2*$^{fl/fl}$*Foxp3*$^{YFP\text{-}Cre}$ (*n*=5) mice. (**B**) Tumor mass of control (*n*=14) and *Prkaa1/2*$^{fl/fl}$*Foxp3*$^{YFP\text{-}Cre}$
883 (*n*=10) mice at day 15 post-engraftment. (**C**) Ratio of live CD8+ cell counts to live CD4+*Foxp3*^{YFP}+
884 (Treg) cell counts in B16 melanoma tumors of control (*n*=19) and *Prkaa1/2*$^{fl/fl}$*Foxp3*$^{YFP\text{-}Cre}$ (*n*=19) mice
885 at day 15 post-engraftment. (**D**) Absolute counts of CD8^{+} Tconv cells and Treg cells per mg of tumor
886 from control (*n*=14, CD8+ Tconv cells; *n*=6, Treg cells) and *Prkaa1/2*$^{fl/fl}$*Foxp3*$^{YFP\text{-}Cre}$ mice (*n*=15, CD8+
887 Tconv cells; *n*=6, Treg cells). (**E**) *K*-means clustering of differentially expressed genes (FDR $q < 0.05$)
888 identified between Treg cells sorted from B16 melanoma tumors of control (*n*=5) and
889 *Prkaa1/2*$^{fl/fl}$*Foxp3*$^{YFP\text{-}Cre}$ (*n*=3) mice at day 15 post-engraftment with *k*=3 and scaled as *z*-scores across
890 rows. (**F**) Average *z*-scores for the three clusters shown in (E). (**G**) *Ppargc1a* expression (*n*=5 control,
891 *n*=3 *Prkaa1/2*$^{fl/fl}$*Foxp3*$^{YFP\text{-}Cre}$). (**H**) Selection of top gene ontology (GO) processes (FDR $q < 0.05$). (**I**) *K*-
892 means clustering of differentially expressed genes (FDR $q < 0.05$) identified between Treg cells sorted
893 from B16 melanoma tumors of control (*n*=6) and *Prkaa1/2*$^{fl/fl}$*Foxp3*$^{YFP\text{-}Cre}$ (*n*=6) mice at day 12 post-
894 engraftment with *k*=2 and scaled as *z*-scores across rows. (**J-K**) GSEA preranked test enrichment plots
895 ($p < 0.05$, FDR $q < 0.25$) of the REACTOME_DNA_METHYLATION (J) and
896 REACTOME_HDACS_DEACETYLATE_HISTONES (K) from tumor-infiltrating *Prkaa1/2*$^{fl/fl}$*Foxp3*$^{YFP\text{-}Cre}$
897 and control Treg cells on day 12 post-engraftment. **** $p < 0.0001$ according to 2-way ANOVA with
898 two-stage linear step-up procedure of Benjamini, Krieger, and Yekutieli with Q = 5% (A). *** $p < 0.001$
899 according to Mann Whitney U test (B, C). One outlier was identified and excluded from (B) and two
900 from (C) using the ROUT method (Q = 0.5%).
901

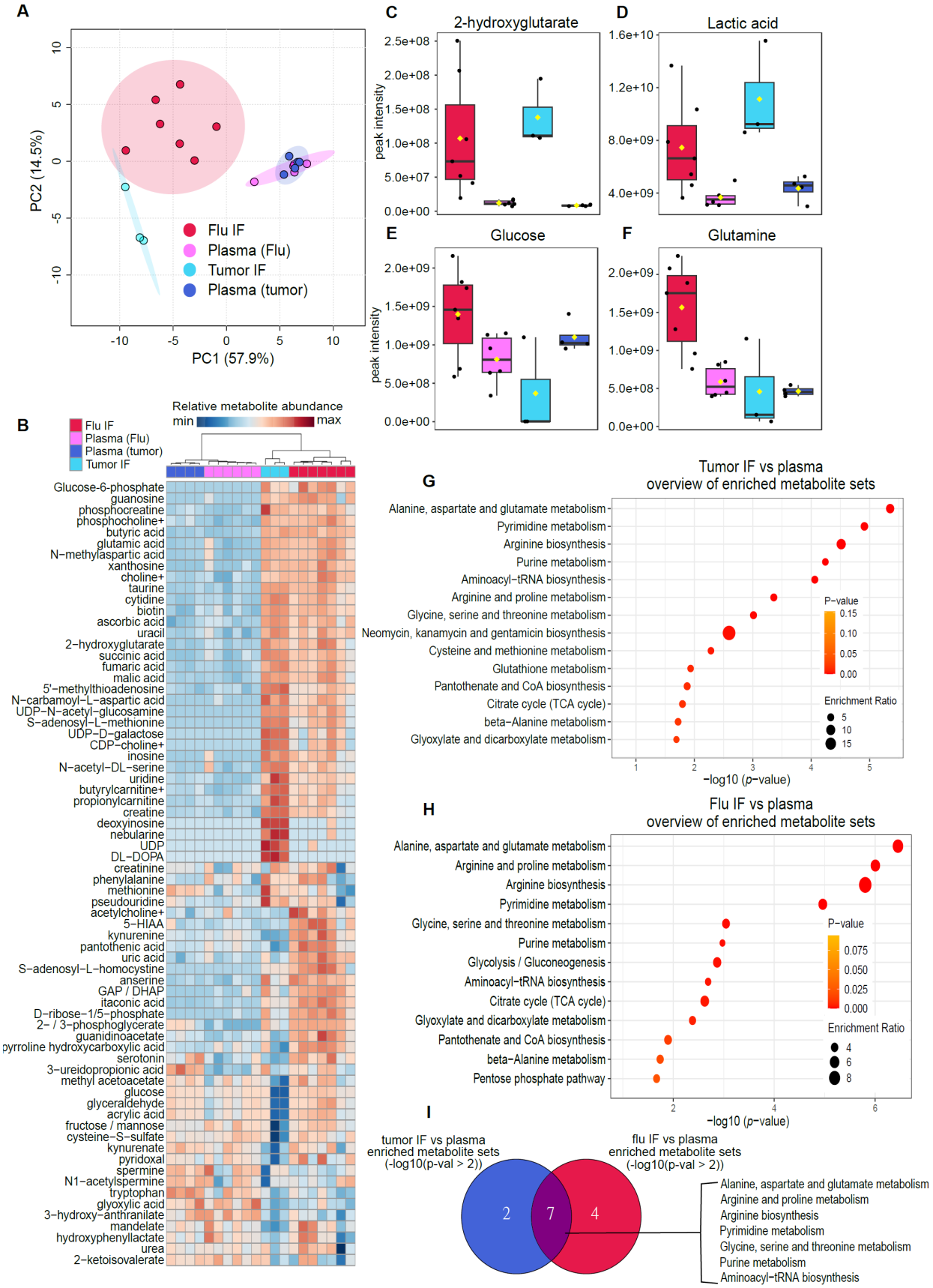

Figure 3. The metabolic landscape of the influenza virus-injured lung resembles the tumor microenvironment in its metabolite abundance; however, they differ in the abundance of key

carbon sources. (**A**) Principal component (PC) analysis of the peak intensities of metabolites identified via liquid chromatography tandem mass spectrometry (LC-MS) from B16 melanoma tumor (n=3) and influenza virus-infected lung (flu, n=7) interstitial fluid (IF) and paired plasma (n=4 tumor, n=6 flu) from the same animals. (**B**) Heatmap of the 70 most differentially represented metabolites in plasma, tumor IF, and flu IF according to one-way ANOVA ($p < 0.1$). (**C-F**) Abundance of key significant differentially represented metabolites: 2-hydroxyglutarate (C), lactic acid (D), glucose (E), and glutamine (F). (**G**) Results from overrepresentation analysis of the significant ($p < 0.1$) differentially represented metabolites between tumor IF and plasma. (**H**) Results from overrepresentation analysis of the significant ($p < 0.1$) differentially represented metabolites between flu IF and plasma. (**I**) Overlap in significantly ($p < 0.1$) enriched metabolite sets between tumor IF vs plasma comparison and flu IF vs plasma comparison according to overrepresentation analysis of flu IF versus plasma and tumor IF versus plasma.

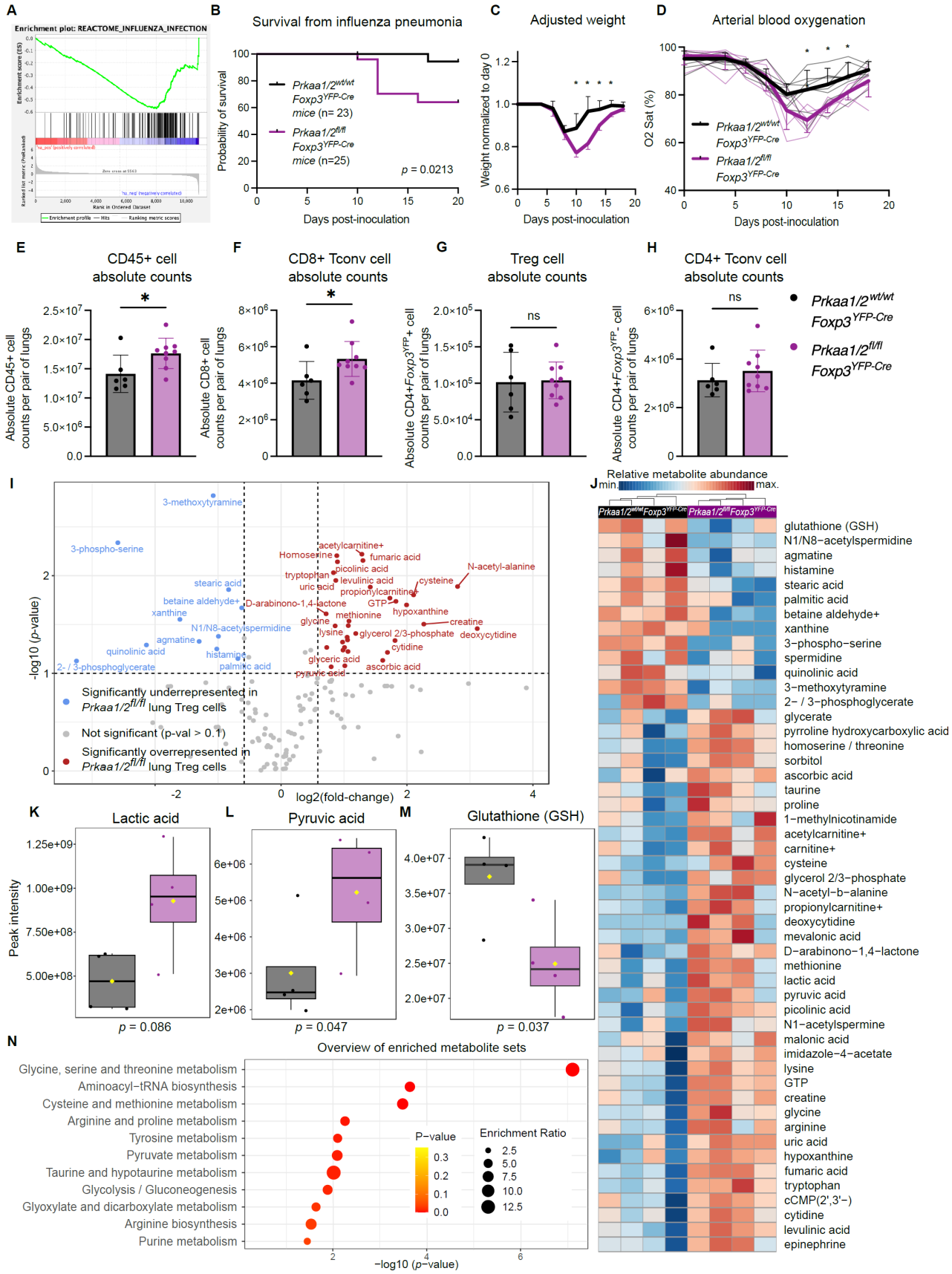

Figure 4. AMPKα1/α2 are necessary for optimal Treg cell function in the lung during influenza pneumonia. (**A**) Enrichment plot of the REACTOME_INFLUENZA_INFECTION geneset ($p < 0.05$,

922 FDR q < 0.25) generated through GSEA preranked testing of the expressed genes of
923 *Prkaa1/2*$^{wt/wt}$*Foxp3*$^{YFP\text{-}Cre}$ (control) and *Prkaa1/2*$^{fl/fl}$*Foxp3*$^{YFP\text{-}Cre}$ CD4+*Foxp3*^{YFP}+ splenocytes identified
924 by RNA-sequencing shown in Figure 1K. (**B**) Survival of control (n=23) and *Prkaa1/2*$^{fl/fl}$*Foxp3*$^{YFP\text{-}Cre}$
925 (n=25) mice following intra-tracheal inoculation of 12.5 plaque forming units (PFUs) of influenza
926 A/WSN/33 H1N1 (influenza) virus. (**C**-**D**) Weight (C), and arterial oxyhemoglobin saturation (D) over
927 time of control (n=6) and *Prkaa1/2*$^{fl/fl}$*Foxp3*$^{YFP\text{-}Cre}$ (n=8) mice following intra-tracheal inoculation of 12.5
928 PFUs of influenza virus. (**E**-**H**) Absolute counts of CD45+ cells (E), CD8+ cells (F), CD4+*Foxp3*^{YFP}+
929 cells (G), and CD4+ cells (H) per pair of lungs in control (n=6) and *Prkaa1/2*$^{fl/fl}$*Foxp3*$^{YFP\text{-}Cre}$ (n=9) mice
930 at day 10 post-influenza virus inoculation. (**I**) Volcano plot of abundance of metabolites detected in
931 control (n=4) and *Prkaa1/2*$^{fl/fl}$*Foxp3*$^{YFP\text{-}Cre}$ (n=4) Treg cells sorted from lungs at day 10 post-influenza
932 virus-inoculation. (**J**) Heatmap of top 50 differentially represented metabolites between control (n=4)
933 and *Prkaa1/2*$^{fl/fl}$*Foxp3*$^{YFP\text{-}Cre}$ (n=4) Treg cells sorted from lungs at day 10 post-influenza virus
934 inoculation. (**K**-**M**) Peak intensities measured for lactic acid (K), pyruvic acid (L), and glutathione GSH
935 (M) in Treg cells from the lungs of control (n=4) and *Prkaa1/2*$^{fl/fl}$*Foxp3*$^{YFP\text{-}Cre}$ (n=4) mice at day 10 post-
936 influenza virus-inoculation. (**N**) Results of overrepresentation analysis from the significant (p < 0.1,
937 $\log_2$(fold-change) ≥ 1.5 or ≤ -1.5) differentially represented metabolites identified in (I). Survival curve
938 (B) p was determined using log-rank (Mantel-Cox) test. * q < 0.05 according to two-way ANOVA with
939 two-stage linear step-up procedure of Benjamini, Krieger, and Yekutieli with Q = 5% (C-D). * p < 0.05,
940 ns not significant according to Mann-Whitney U test (E-H).
941

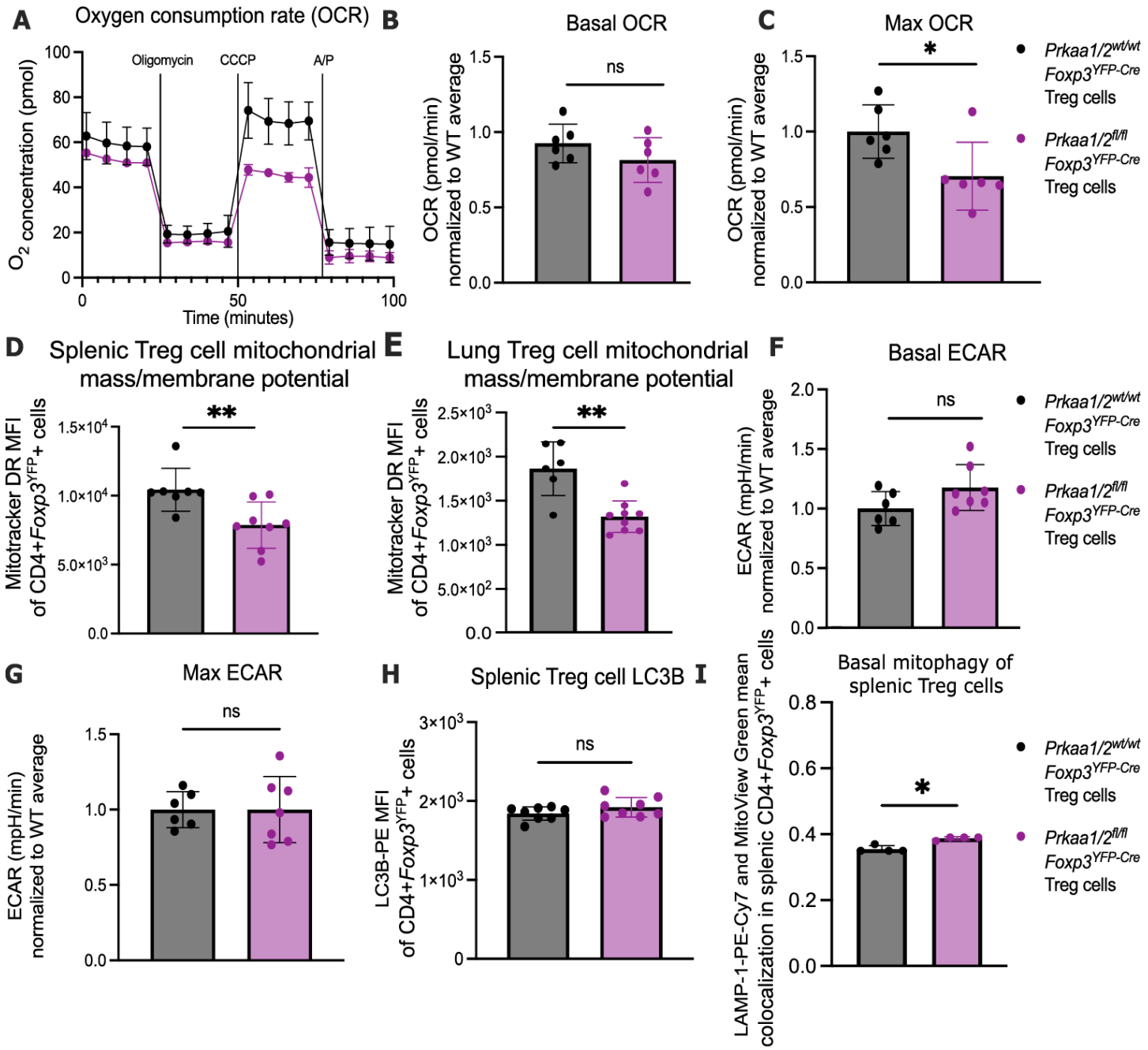

Figure 5. AMPKα is necessary for maximal Treg cell mitochondrial function. (**A**) Representative oxygen consumption rate (OCR) over time of CD4+*Foxp3*^{YFP}+ splenocytes from *Prkaa1/2*$^{wt/wt}$*Foxp3*$^{YFP\text{-}Cre}$ (control, *n*=3) and *Prkaa1/2*$^{fl/fl}$*Foxp3*$^{YFP\text{-}Cre}$ (*n*=2) mice following treatment of oligomycin (2.5 μM), carbonyl cyanide m-chlorophenylhydrazone (CCCP; 10 μM), and antimycin A/piercidin (A/P; 2 μM each) as measured by a metabolic flux assay. (**B**-**C**) Basal (B) and maximal (C) OCR of CD4+*Foxp3*^{YFP}+ splenocytes from control (*n*=6) and *Prkaa1/2*$^{fl/fl}$*Foxp3*$^{YFP\text{-}Cre}$ (*n*=6) mice, some of which are shown in (A). (**D**-**E**) MitoTracker Deep Red (MitoTracker DR) mean fluorescence intensity (MFI) of CD4+*Foxp3*^{YFP}+ splenocytes at homeostasis (D; *n*=7 control, *n*=8 *Prkaa1/2*$^{fl/fl}$*Foxp3*$^{YFP\text{-}Cre}$ mice) and lung CD4+*Foxp3*^{YFP}+ cells at day 10 post-influenza virus inoculation (E; same cohort as in Figure 4E-H and Supplemental Figure 7, *n*=6 control, *n*=9 *Prkaa1/2*$^{fl/fl}$*Foxp3*$^{YFP\text{-}Cre}$ mice). (**F**-**G**) Basal (F) and maximal (G) extracellular acidification rate (ECAR) of CD4+*Foxp3*^{YFP}+ splenocytes from control (*n*=6) and *Prkaa1/2*$^{fl/fl}$*Foxp3*$^{YFP\text{-}Cre}$ (*n*=7) mice. (**H**) LC3B-PE MFI of CD4+*Foxp3*^{YFP}+ splenocytes from control

955 (*n*=8) and *Prkaa1/2*$^{fl/fl}$*Foxp3*$^{YFP\text{-}Cre}$ (*n*=8) mice. (**I**) Mean LAMP-1-PE-Cy7 and MitoView Green co-
956 localization in CD4+*Foxp3*^{YFP}+ splenocytes from control (*n*=4) and *Prkaa1/2*$^{fl/fl}$*Foxp3*$^{YFP\text{-}Cre}$ (*n*=4) mice.
957 * $p < 0.05$, ** $p < 0.01$, ns not significant according to Mann-Whitney *U* test.
958

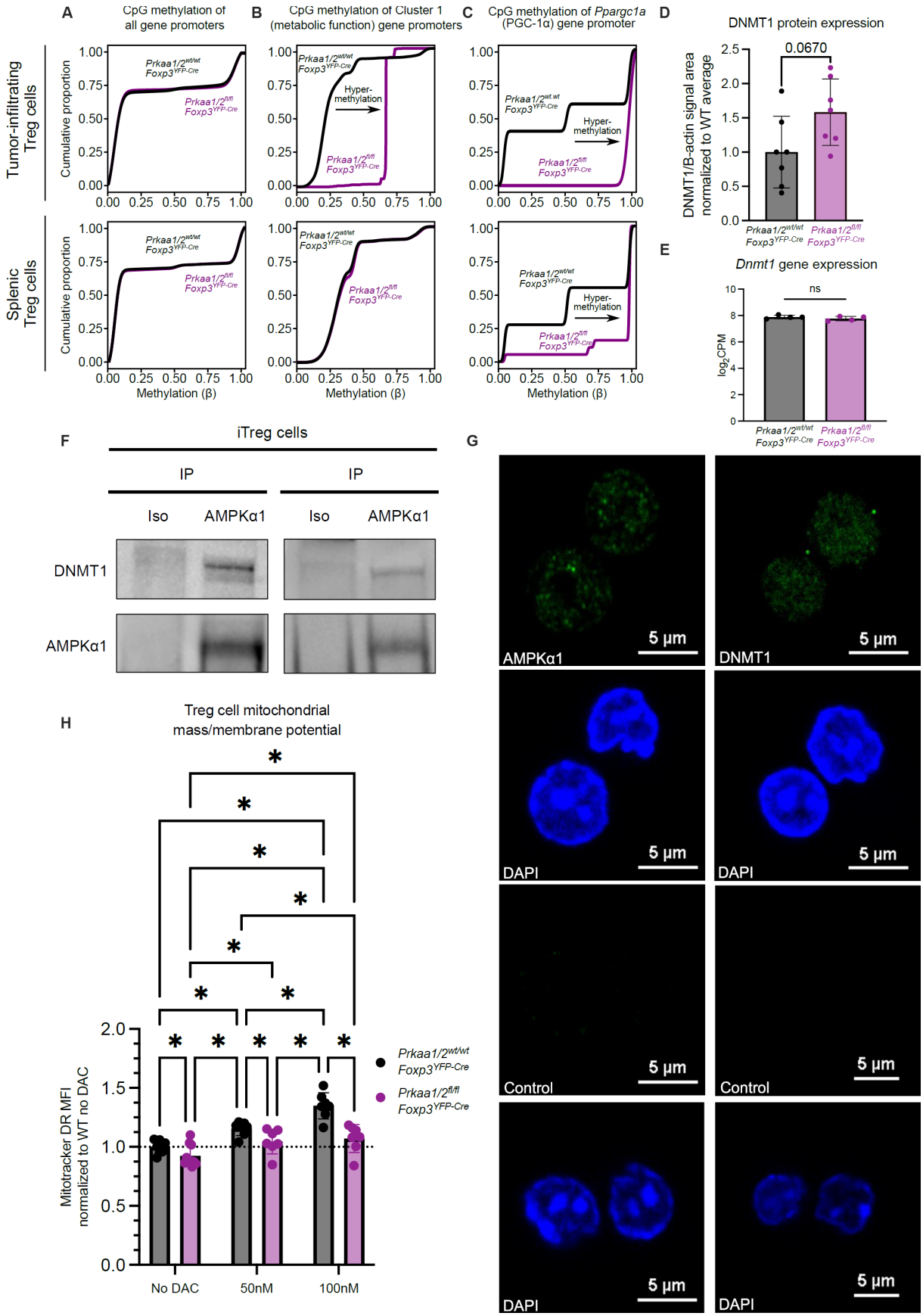

Figure 6. AMPKα1 interacts with DNMT1 to demethylate the promoter of mitochondrial genes in tumor-infiltrating Treg cells. (**A-C**) CpG methylation of all gene promoters (A), gene promoters of

962 cluster 1 genes identified by *k*-means clustering of the RNA-sequencing shown in Figure 2E (B), and
963 the *Ppargc1a* promoter (C) in tumor-infiltrating CD4+*Foxp3*^{YFP}+ cells (*n*=4 *Prkaa1/2*$^{wt/wt}$*Foxp3*$^{YFP\text{-}Cre}$ or
964 control, *n*=2 *Prkaa1/2*$^{fl/fl}$*Foxp3*$^{YFP\text{-}Cre}$) and splenic CD4+*Foxp3*^{YFP}+ cells at homeostasis (*n*=3 control,
965 *n*=3 *Prkaa1/2*$^{fl/fl}$*Foxp3*$^{YFP\text{-}Cre}$) (**D**) DNMT1 protein expression of splenic CD4+*Foxp3*^{YFP}+ (Treg) cells at
966 homeostasis (*n*=7 control, *n*=7 *Prkaa1/2*$^{fl/fl}$*Foxp3*$^{YFP\text{-}Cre}$). Three independent experiments are shown.
967 DNMT1 peak intensity area was normalized to the corresponding sample's β-actin peak intensity area.
968 (**E**) *Dnmt1* gene expression of splenic CD4+*Foxp3*^{YFP}+ cells at homeostasis (*n*=4 control, *n*=4
969 *Prkaa1/2*$^{fl/fl}$*Foxp3*$^{YFP\text{-}Cre}$) as measured by RNA-sequencing shown in Figure 1. (**F**) Anti-AMPKα1 and
970 isotype control immunoprecipitates from ex vivo induced (i)Treg cell lysates blotted for DNMT1 protein.
971 Independent biological replicates are shown. (**G**) Representative microscopy images of AMPKα-
972 sufficient iTreg cells showing AMPKα1 and DNMT1 subcellular localization. (**H**) MitoTracker Deep Red
973 (MitoTracker DR) mean fluorescence intensity (MFI) of AMPKα-sufficient (control) and -deficient splenic
974 CD4+*Foxp3*^{YFP}+ cells treated with either vehicle (*n*=8 control, *n*=10 *Prkaa1/2*$^{fl/fl}$*Foxp3*$^{YFP\text{-}Cre}$), 50 nM
975 decitabine (DAC, *n*=7 control, *n*=7 *Prkaa1/2*$^{fl/fl}$*Foxp3*$^{YFP\text{-}Cre}$), or 100 nM DAC (*n*=7 control, *n*=7
976 *Prkaa1/2*$^{fl/fl}$*Foxp3*$^{YFP\text{-}Cre}$). * *p or q* < 0.05, ns not significant according to Mann-Whitney *U* test (D-E) with
977 two-stage linear step-up procedure of Benjamini, Krieger, and Yekutieli with Q = 5% (H).
978

979

	Allele	Primer direction	Primer sequence
Genotyping primers	*Prkaa1*^{fl}	Forward	GCAGCCCAATTCCGATCATATTCA
		Reverse	GCCTGCTTTGCACACTTATGG
	Prkaa1^{wt}	Forward	CGACTAGCTTCATGTCCTGTTTTCT
		Reverse	CCTGCTTGGCACACTTATGGTAA
	Prkaa2^{fl}	Forward	GCAGCCCAATTCCGATCATATTCA
		Reverse	TGGAACATCTTTTAGACAGAATAATCTTTTAGACAG
	Prkaa2^{wt}	Forward	CGAAAAACTCAAAAAAATTATTATTCTGTAATAGATAGTGATGTTAAA
		Reverse	CCTTCATTAGAATACTATGGAACATCTTTTAGACA

RT-PCR primers	*Prkaa1*^{wt}	Forward	GCTGTGGCTCACCCAATTAT
		Reverse	TGTTGTACAGGCAGCTGAGG
	Prkaa2^{wt}	Forward	CGGCTCTTTCAGCAGATTCTGT
		Reverse	ATCGGCTATCTTGGCATTCATG

980
981 **Supplemental Table 1.** Primer sequences used to genotype and profile the expression of the *Prkaa1*
982 and *Prkaa2* loci.
983

984

Antigen/Reagent	Conjugate	Clone	Manufacturer	Catalog no.
CD45	BUV563	30-F11	BD Horizon	612924
CD4	BUV395	GK1.5	BD Horizon	563790
CD8	BUV805	53-6.7	BD Horizon	612898
CD8	BV711	53-6.7	Biolegend	100747
CD25	BV605	PC61	Biolegend	102036
CD25	APC	PC61.5	Invitrogen	2154040
CD62L	APC-e780	MEL-14	Invitrogen	2011195
CD44	BUV737	IM7	BD Horizon	564392
PD-1	PE/Dazzle594	RMP1-30	Biolegend	109116
PD-1	PerCP-eFluor710	J43	Invitrogen	46-9985-82
CTLA-4	BV421	UC10-4B9	Biolegend	106312
TIGIT	BV711	1G9	BD Biosciences	744214
ICOS	BV786	C398.4A	BD Biosciences	567922
Ki-67	Alexa Fluor 488	11F6	Biolegend	151204
FOXP3	PE-Cy7	FJK-16s	BD Biosciences	25-5773-82
LC3B	PE	D11	Biolegend	8899S
LAMP-1	PE-Cy7	1D4B	eBioscience	25-1071-82
Fixable Viability Dye eFluor506	N/A	N/A	eBioscience	65-0866-14
Cell Trace Violet	N/A	N/A	Invitrogen	C34571
Absolute counting beads	N/A	N/A	Invitrogen	C36950
Mitotracker Deep Red	N/A	N/A	Invitrogen	M22426
MitoView Green	N/A	N/A	Biotium	70054

985

986 **Supplemental Table 2. Flow cytometry fluorochromes and reagents.** Fixable viability dye eFluor
987 506, cell trace violet, and absolute counting beads were used according to manufacturer instructions.
988 MitoTracker Deep Red staining: After surface marker fluorochrome stain, single-cell suspensions
989 were stained with 50 nM MitoTracker Deep Red in complete RPMI for 30 minutes at 37 °C.
990

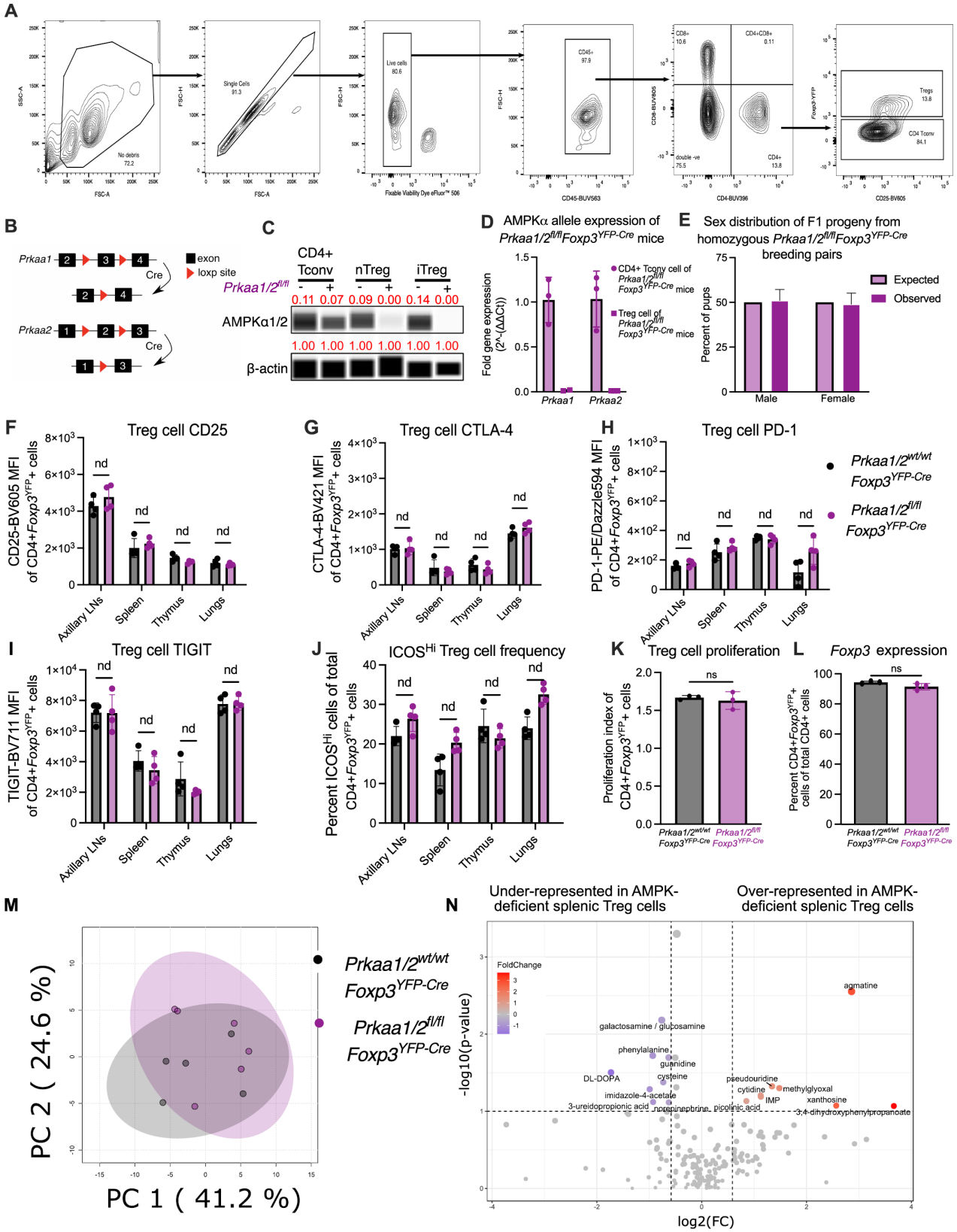

Supplemental Figure 1. Validation of AMPKα1/α2 conditional knockout and Treg cell and mouse phenotyping of *Prkaa1/2$^{fl/fl}$Foxp3$^{YFP\text{-}Cre}$* and control mice. (**A**) Flow cytometry gating strategy for

phenotyping of T cell populations, including CD4+*Foxp3*^{YFP}+ (Treg) cells. (**B**) Schematic of the *Foxp3*$^{YFP\text{-}Cre}$-mediated excision of loxP-flanked exons of *Prkaa1* and *Prkaa2* in Treg cells. (**C**) Validation of Treg cell-specific knockout of AMPKα1/α2 using the Simple Wes immunoassay system (*n*=3 replicates per group and cell type pooled and run as single well); signal intensities normalized to the corresponding lane's β-actin signal in red. (**D**) Relative expression of *Prkaa1* and *Prkaa2* by CD4+*Foxp3*^{YFP}- T (CD4+ Tconv) cells and Treg cells of *Prkaa1/2*$^{fl/fl}$*Foxp3*$^{YFP\text{-}Cre}$ mice (*n*=3 Tconv cells, *n*=2 Treg cells). (**E**) Observed and expected frequencies of F1 pups from crosses of male *Prkaa1/2*$^{fl/fl}$*Foxp3*$^{YFP\text{-}Cre/Y}$ mice with female *Prkaa1/2*$^{fl/fl}$*Foxp3*$^{YFP\text{-}Cre/YFP\text{-}Cre}$ mice. Chi-square test for goodness of fit p = 0.75. Chi-square = 0.1 with 1 degree of freedom (n=127 males and 122 females). (**F-I**) CD25-BV605 (F), CTLA-4-BV421 (G), PD-1-PE/Dazzle594 (H), and TIGIT-BV711 (I) mean fluorescence intensity (MFI) of Treg cells from *Prkaa1/2*$^{wt/wt}$*Foxp3*$^{YFP\text{-}Cre}$ (control) and *Prkaa1/2*$^{fl/fl}$*Foxp3*$^{YFP\text{-}Cre}$ mouse axillary lymph nodes (LN), spleen, thymus, and lung (*n*=4 control, *n*=4 *Prkaa1/2*$^{fl/fl}$*Foxp3*$^{YFP\text{-}Cre}$). (**J**) Frequency of ICOS^{Hi} CD4+*Foxp3*^{YFP}+ cells of total CD4+*Foxp3*^{YFP}+ cells from control and *Prkaa1/2*$^{fl/fl}$*Foxp3*$^{YFP\text{-}Cre}$ mouse LN, spleen, thymus, and lung (*n*=4 control, *n*=4 *Prkaa1/2*$^{fl/fl}$*Foxp3*$^{YFP\text{-}Cre}$). (**K**) Proliferation index of Cell Trace Violet+ CD4+*Foxp3*^{YFP}+ cells according to FlowJo 10.9.0's proliferation modeling tool (*n*=3 control, *n*=3 *Prkaa1/2*$^{fl/fl}$*Foxp3*$^{YFP\text{-}Cre}$). (**L**) Frequency of CD4+*Foxp3*^{YFP}+ cells of total CD4+ cells after in vitro treatment of CD4+Foxp3- splenocytes with Treg cell-polarizing conditions for 5 days (*n*=3 control, *n*=3 *Prkaa1/2*$^{fl/fl}$*Foxp3*$^{YFP\text{-}Cre}$). (**M-N**) Principal component (PC) analysis (M) and volcano plot (N) of LC-MS data generated with metabolites extracted from splenic Treg cells of control (*n*=5) and *Prkaa1/2*$^{fl/fl}$*Foxp3*$^{YFP\text{-}Cre}$ (*n*=6) mice. ns not significant, nd no discovery according to Mann-Whitney *U* test (K-L) with two-stage linear step-up procedure of Benjamini, Krieger, and Yekutieli with Q = 5% (F-J).

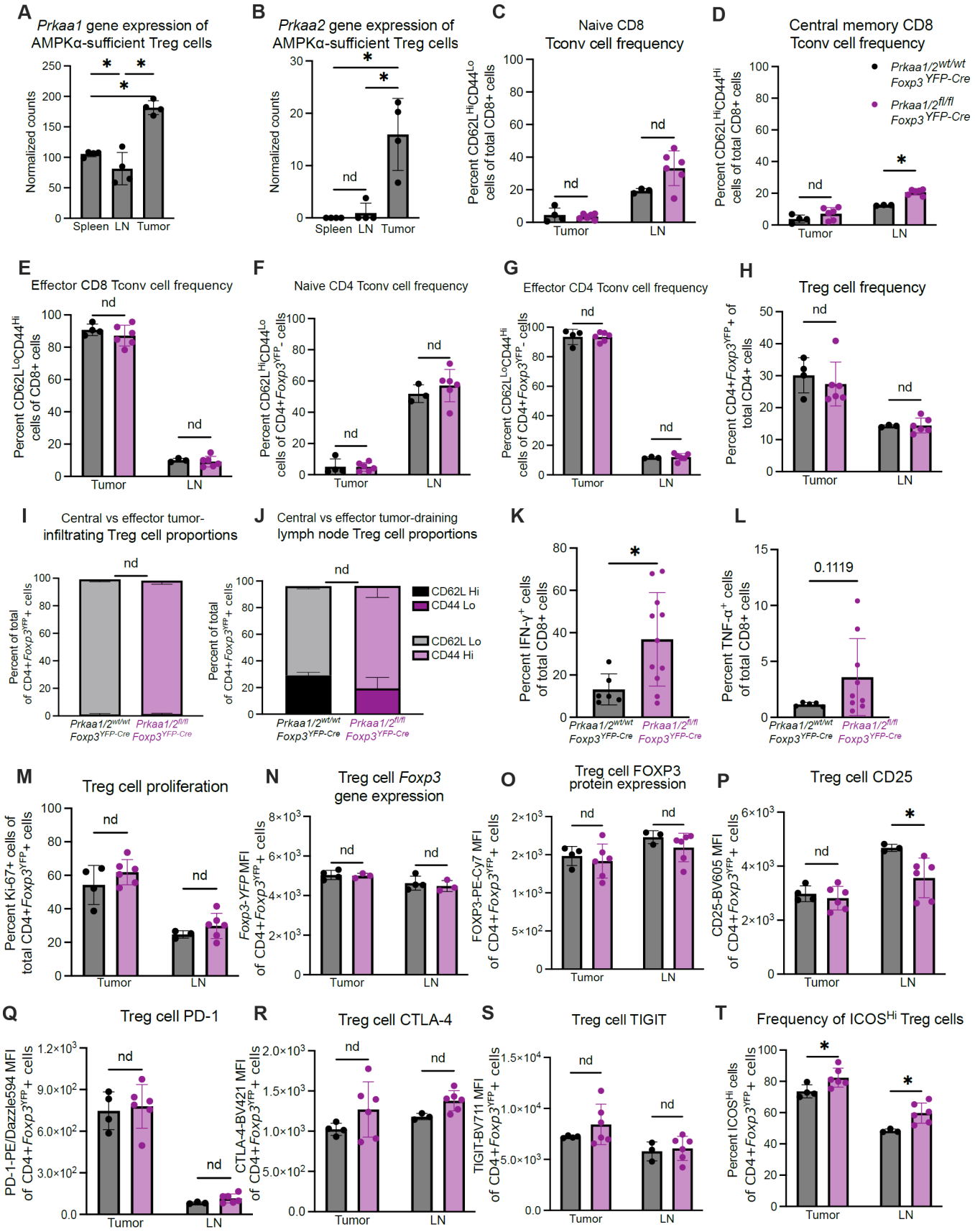

Supplemental Figure 2. Immune phenotyping of tumor-infiltrating T cell subsets of *Prkaa1/2$^{fl/fl}$Foxp3$^{YFP\text{-}Cre}$* and control mice. (**A-B**) Normalized gene expression counts of *Prkaa1* (A)

and *Prkaa2* (B) by CD4+*Foxp3*^{YFP}+ cells sorted from tumors, spleens, and lymph nodes of tumor-bearing *Prkaa1/2*$^{wt/wt}$*Foxp3*$^{YFP\text{-}Cre}$ (control, *n*=4) mice. (**C**-**E**) Frequency of naive (CD62L^{Hi}CD44^{Lo}; C), central memory (CD62L^{Hi}CD44^{Hi}; D), and effector (CD62L^{Lo}CD44^{Hi}; E) CD8+ conventional T (Tconv) cells out of total CD8+ cells in tumors (*n*=4 control, *n*=6 *Prkaa1/2*$^{fl/fl}$*Foxp3*$^{YFP\text{-}Cre}$) and tumor-draining lymph nodes (LN; *n*=3 control, *n*=6 *Prkaa1/2*$^{fl/fl}$*Foxp3*$^{YFP\text{-}Cre}$ mice). (**F**-**G**) Frequency of naive (F) and effector (G) Effector Tconv cells out of total CD4+*Foxp3*^{YFP}- cells in tumors (*n*=4 control, *n*=6 *Prkaa1/2*$^{fl/fl}$*Foxp3*$^{YFP\text{-}Cre}$ mice) and LN (*n*=3 control, *n*=6 *Prkaa1/2*$^{fl/fl}$*Foxp3*$^{YFP\text{-}Cre}$ mice). (**H**) Percent of CD4+*Foxp3*^{YFP}+ cells out of total CD4+ cells in tumors (*n*=4 control, *n*=6 *Prkaa1/2*$^{fl/fl}$*Foxp3*$^{YFP\text{-}Cre}$ mice) and LN (*n*=3 control, *n*=6 *Prkaa1/2*$^{fl/fl}$*Foxp3*$^{YFP\text{-}Cre}$ mice). (**I**-**J**) Frequency of central (CD62L^{Hi}CD44^{Lo}) and effector (CD62L^{Lo}CD44^{Hi}) CD4+*Foxp3*^{YFP}+ cells out of total CD4+*Foxp3*^{YFP}+ cells in tumors (I; *n*=4 control, *n*=6 *Prkaa1/2*$^{fl/fl}$*Foxp3*$^{YFP\text{-}Cre}$ mice) and LN (J; *n*=3 control, *n*=6 *Prkaa1/2*$^{fl/fl}$*Foxp3*$^{YFP\text{-}Cre}$ mice). (**K**-**L**) Frequency of IFN-γ+ (*n*=6 control, *n*=11 *Prkaa1/2*$^{fl/fl}$*Foxp3*$^{YFP\text{-}Cre}$ mice) (K) and TNF-α+ (*n*=5 control, *n*=9 *Prkaa1/2*$^{fl/fl}$*Foxp3*$^{YFP\text{-}Cre}$ mice) (L) cells of total CD8+ T cells (**M**) Frequency of Ki-67+CD4+*Foxp3*^{YFP}+ cells out of total CD4+*Foxp3*^{YFP}+ cells in tumors (*n*=4 control, *n*=6 *Prkaa1/2*$^{fl/fl}$*Foxp3*$^{YFP\text{-}Cre}$ mice) and LN (*n*=3 control, *n*=6 *Prkaa1/2*$^{fl/fl}$*Foxp3*$^{YFP\text{-}Cre}$ mice). (**N**) *Foxp3*^{YFP} mean fluorescence intensity (MFI) of CD4+*Foxp3*^{YFP}+ cells in tumors (*n*=4 control, *n*=6 *Prkaa1/2*$^{fl/fl}$*Foxp3*$^{YFP\text{-}Cre}$ mice) and LN (*n*=3 control, *n*=6 *Prkaa1/2*$^{fl/fl}$*Foxp3*$^{YFP\text{-}Cre}$ mice). (**O**-**S**) FOXP3-PE-Cy7 (O), CD25-BV605 (P), PD-1-PE/Dazzle594 (Q), CTLA-4-BV421 (R) and TIGIT-BV711 (S) MFI of CD4+*Foxp3*^{YFP}+ cells from tumors (*n*=4 control, *n*=6 *Prkaa1/2*$^{fl/fl}$*Foxp3*$^{YFP\text{-}Cre}$ mice) and LN (*n*=3 control, *n*=6 *Prkaa1/2*$^{fl/fl}$*Foxp3*$^{YFP\text{-}Cre}$ mice). (**T**) Frequency of ICOS^{Hi} CD4+*Foxp3*^{YFP}+ cells out of total CD4+*Foxp3*^{YFP}+ cells in tumors (*n*=4 control, *n*=6 *Prkaa1/2*$^{fl/fl}$*Foxp3*$^{YFP\text{-}Cre}$ mice) and LN (*n*=3 control, *n*=6 *Prkaa1/2*$^{fl/fl}$*Foxp3*$^{YFP\text{-}Cre}$ mice). * $q < 0.05$, nd no discovery according to Mann Whitney U test (K-L) with two-stage linear step-up procedure of Benjamini, Krieger, and Yekutieli with Q = 5% (A-J,M-T). Four outliers identified and excluded from (L) using the ROUT method (Q=1%).

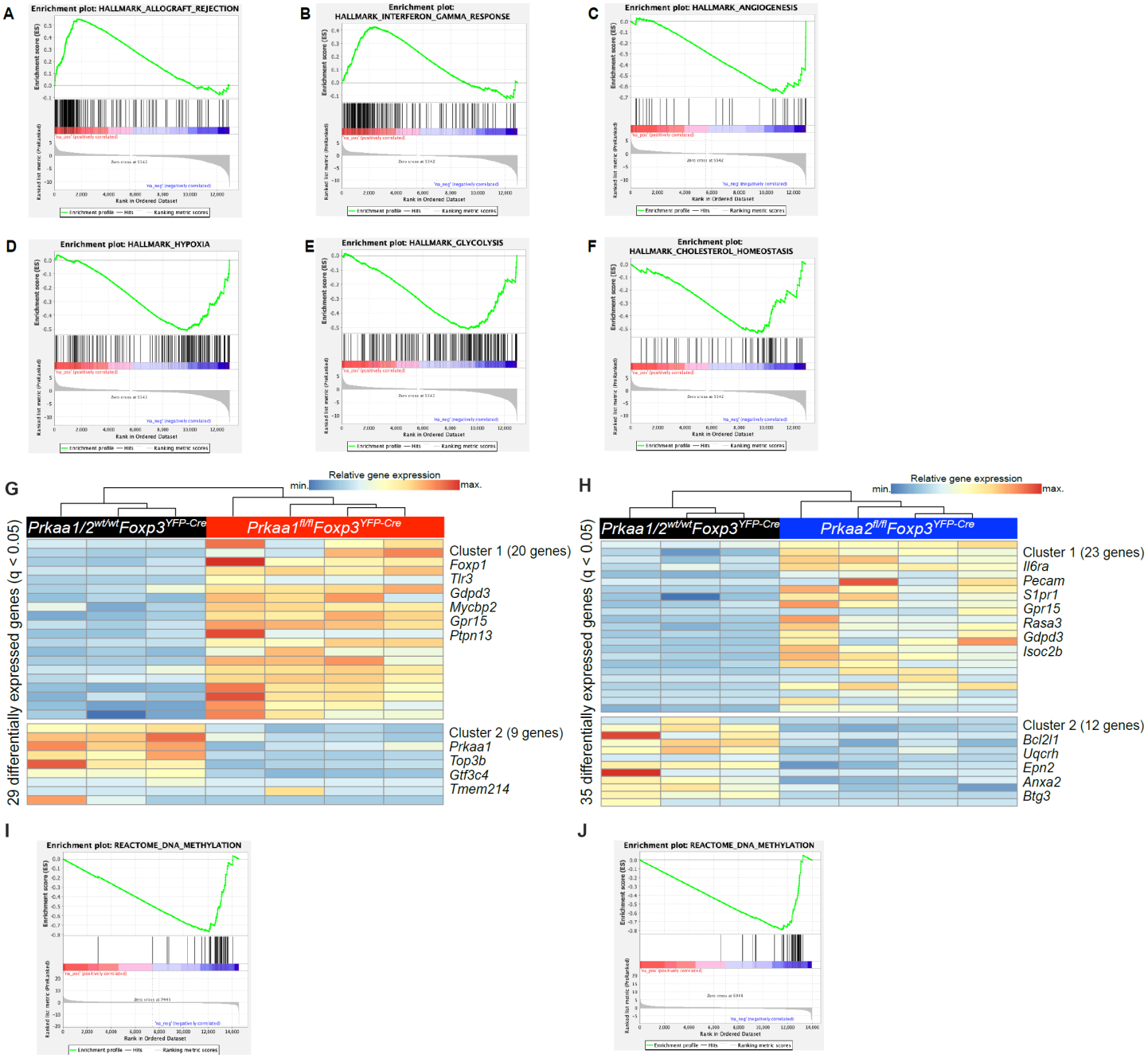

Supplemental Figure 3. Transcriptional phenotyping of tumor-infiltrating AMPKα1/α2-deficient, AMPKα1-deficient, AMPKα2-deficient, and control Treg cells at day 12 post-engraftment. (**A-F**) Enrichment plots ($p < 0.05$, FDR $q < 0.25$) of the HALLMARK_ALLOGRAFT_REJECTION (A), HALLMARK_INTERFERON_GAMMA_RESPONSE (B), HALLMARK_ANGIOGENESIS (C), HALLMARK_HYPOXIA (D), HALLMARK_GLYCOLYSIS (E), and HALLMARK_CHOLESTEROL HOMEOSTASIS (F) gene sets. Enrichment plots were generated through GSEA preranked testing of the expressed genes of tumor-infiltrating *Prkaa1/2*$^{fl/fl}$*Foxp3*$^{YFP\text{-}Cre}$ and control Treg cells identified by RNA-sequencing at day 15 post-engraftment. (**G-H**) *K*-means clustering of significant differentially expressed genes (FDR $q < 0.05$) identified between Treg cells sorted from B16 melanoma tumors of *Prkaa1*$^{fl/fl}$*Foxp3*$^{YFP\text{-}Cre}$ (n=4) mice versus controls (G) and *Prkaa2*$^{fl/fl}$*Foxp3*$^{YFP\text{-}Cre}$ (n=4) mice versus controls (H) at day 12 post-engraftment, with k=2 and scaled as Z-scores across rows. (**I-J**) Enrichment plots ($p < 0.05$, FDR $q < 0.25$) of the REACTOME_DNA_METHYLATION gene set generated through

058 GSEA preranked testing of the expressed genes of tumor-infiltrating *Prkaa1*$^{fl/fl}$*Foxp3*$^{YFP\text{-}Cre}$ and control
059 Treg cells (G) as well as *Prkaa2*$^{fl/fl}$*Foxp3*$^{YFP\text{-}Cre}$ and control Treg cells (H) identified on day 12 post-
060 engraftment RNA-sequencing.
061

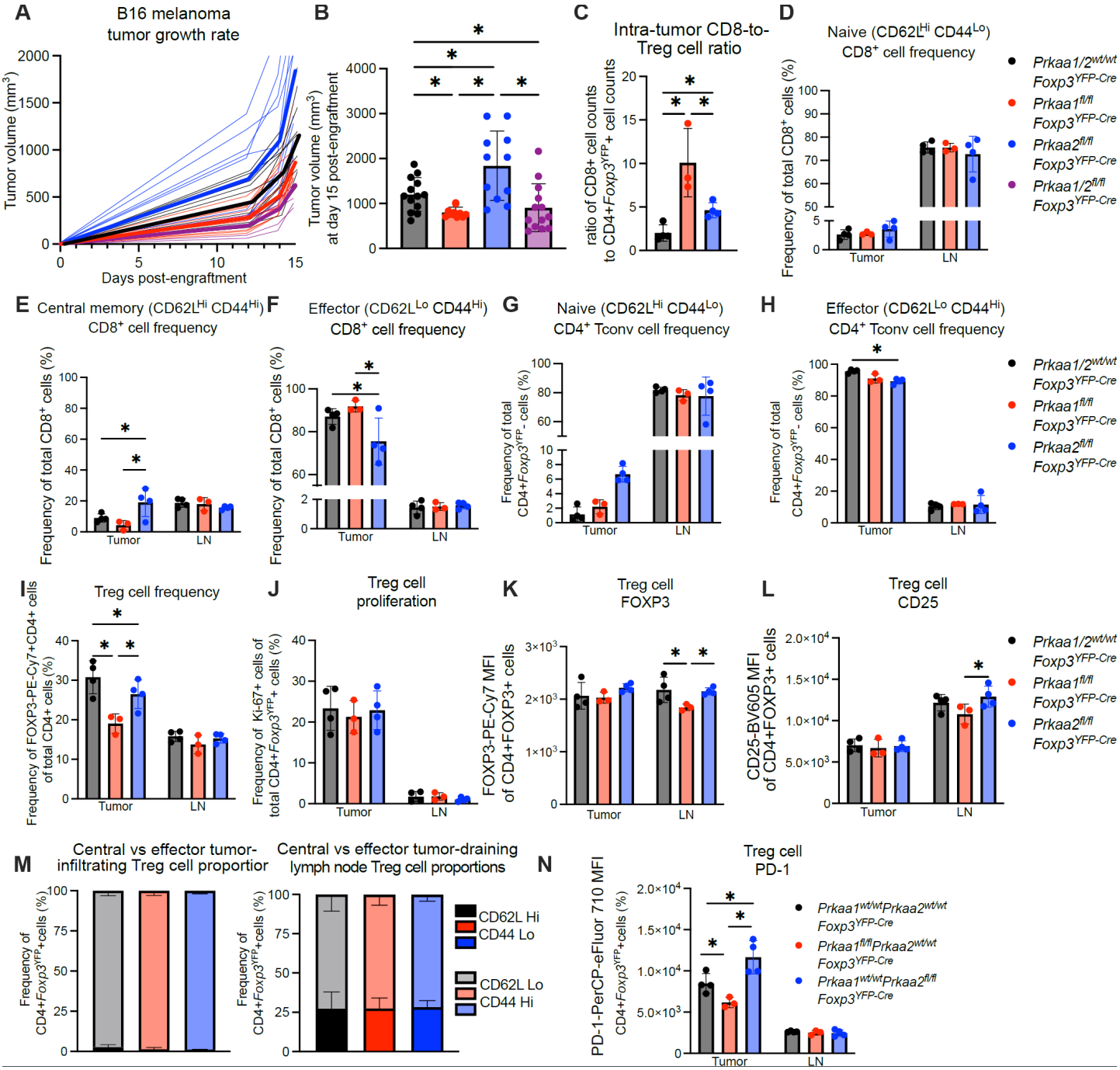

Supplemental Figure 4. The AMPKα1 and AMPKα2 isoforms have differential contribution to Treg cell suppressive function in the TME. (**A-B**)Growth of B16 melanoma tumors (A) and tumor volume at day 15 post-engraftment (B) of *Prkaa1/2*$^{wt/wt}$*Foxp3*$^{YFP\text{-}Cre}$ mice (control, *n*=20; includes replicates from Figure 2A-B), *Prkaa1*$^{fl/fl}$*Foxp3*$^{YFP\text{-}Cre}$ mice (*n*=10), *Prkaa2*$^{fl/fl}$*Foxp3*$^{YFP\text{-}Cre}$ mice (*n*=11), and *Prkaa1/2*$^{fl/fl}$*Foxp3*$^{YFP\text{-}Cre}$ mice (*n*=17; includes replicates from Figure 2A-B). (**C**) Ratio of live CD8+ cell counts to live CD4+*Foxp3*^{YFP}+ cell counts in single-cell suspensions of B16 melanoma tumors harvested from the flanks of control (*n*=4), *Prkaa1*$^{fl/fl}$*Foxp3*$^{YFP\text{-}Cre}$ mice (*n*=3), and *Prkaa2*$^{fl/fl}$*Foxp3*$^{YFP\text{-}Cre}$ mice (*n*=4) at day 15 post-engraftment. (**D-F**) Frequency of naive (CD62L^{Hi}CD44^{Lo}; D), central memory (CD62L^{Hi}CD44^{Hi}; E), and effector (CD62L^{Lo}CD44^{Hi}; F) CD8+ conventional T (Tconv) cells out of total CD8+ cells in tumors and tumor-draining lymph nodes (LN; *n*=4 control, *n*=3 *Prkaa1*$^{fl/fl}$*Foxp3*$^{YFP\text{-}Cre}$, *n*=4 *Prkaa2*$^{fl/fl}$*Foxp3*$^{YFP\text{-}Cre}$). (**G-H**) Frequency of naïve (G) and effector (H) CD4+*Foxp3*^{YFP}- cells out of total

CD4+*Foxp3*^{YFP}- cells in tumors and LN (*n*=4 control, *n*=3 *Prkaa1*$^{fl/fl}$*Foxp3*$^{YFP\text{-}Cre}$, *n*=4 *Prkaa2*$^{fl/fl}$*Foxp3*$^{YFP\text{-}Cre}$). (**I**) Frequency of CD4+*Foxp3*^{YFP}+ cells out of total CD4+ cells in tumors and LN (*n*=4 control, *n*=3 *Prkaa1*$^{fl/fl}$*Foxp3*$^{YFP\text{-}Cre}$, *n*=4 *Prkaa2*$^{fl/fl}$*Foxp3*$^{YFP\text{-}Cre}$). (**J**) Frequency of Ki-67+CD4+*Foxp3*^{YFP}+ cells out of total CD4+*Foxp3*^{YFP}+ cells in tumors and LN (*n*=4 control, *n*=3 *Prkaa1*$^{fl/fl}$*Foxp3*$^{YFP\text{-}Cre}$, *n*=4 *Prkaa2*$^{fl/fl}$*Foxp3*$^{YFP\text{-}Cre}$). (**K**-**L**) FOXP3-PE-Cy7 (K) and CD25-BV605 (L) mean fluorescence intensity (MFI) of CD4+FOXP3+ cells from tumors and LN (*n*=4 control, *n*=3 *Prkaa1*$^{fl/fl}$*Foxp3*$^{YFP\text{-}Cre}$, *n*=4 *Prkaa2*$^{fl/fl}$*Foxp3*$^{YFP\text{-}Cre}$). (**M**) Frequency of central (CD62L^{Hi}CD44^{Lo}) and effector (CD62L^{Lo}CD44^{Hi}) CD4+*Foxp3*^{YFP}+ cells out of total CD4+*Foxp3*^{YFP}+ cells in tumors and LN (*n*=4 control, *n*=3 *Prkaa1*$^{fl/fl}$*Foxp3*$^{YFP\text{-}Cre}$, *n*=4 *Prkaa2*$^{fl/fl}$*Foxp3*$^{YFP\text{-}Cre}$). (**N**) PD-1-BB700 MFI of CD4+*Foxp3*^{YFP}+ cells in tumors and LN (*n*=4 control, *n*=3 *Prkaa1*$^{fl/fl}$*Foxp3*$^{YFP\text{-}Cre}$, *n*=4 *Prkaa2*$^{fl/fl}$*Foxp3*$^{YFP\text{-}Cre}$). * $q < 0.05$ according to two-way ANOVA of day 15 data from (A) using the two-stage linear step-up procedure of Benjamini, Krieger, and Yekutieli with Q = 5% (B). * $q < 0.05$ according to one-way ANOVA using the two-stage linear step-up procedure of Benjamini, Krieger, and Yekutieli with Q = 5% (C-N). Three outliers were identified and excluded from (B) using the ROUT method (Q=1%).

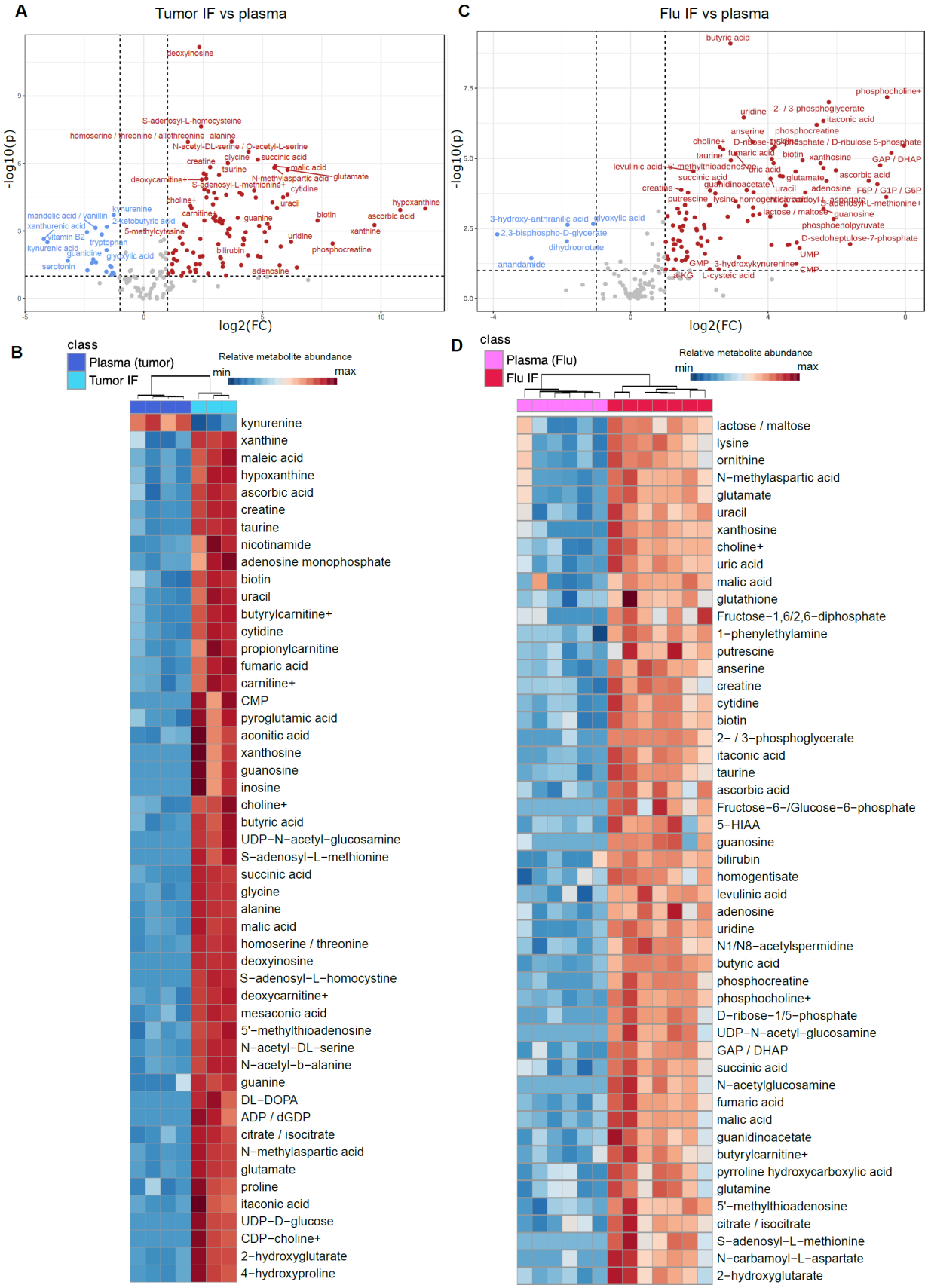

Supplemental Figure 5. Tumor and influenza virus-infected lung interstitial fluid metabolite abundance compared with plasma. (**A**) Volcano plot of abundance of metabolites detected in tumor

093 (*n*=3) interstitial fluid (IF) and paired plasma (*n*=4). Features with $p < 0.1$ were noted in red if $\log_2$(fold-
094 change) ≥ 1.5 or blue if $\log_2$(fold-change) ≤ -1.5 when comparing tumor IF versus plasma. (**B**) Heatmap
095 of top 50 differentially represented metabolites between tumor IF versus plasma. (**C**) Volcano plot of
096 abundance of metabolites detected in influenza virus-infected lung (flu, *n*=7) IF and paired plasma
097 (*n*=6). Features with $p < 0.1$ were noted in red if $\log_2$(fold-change) ≥ 1.5 or blue if $\log_2$(fold-change) ≤ -
098 1.5 when comparing flu IF versus plasma. (**D**) Heatmap of top 50 differentially represented metabolites
099 between flu IF versus plasma.
100

101

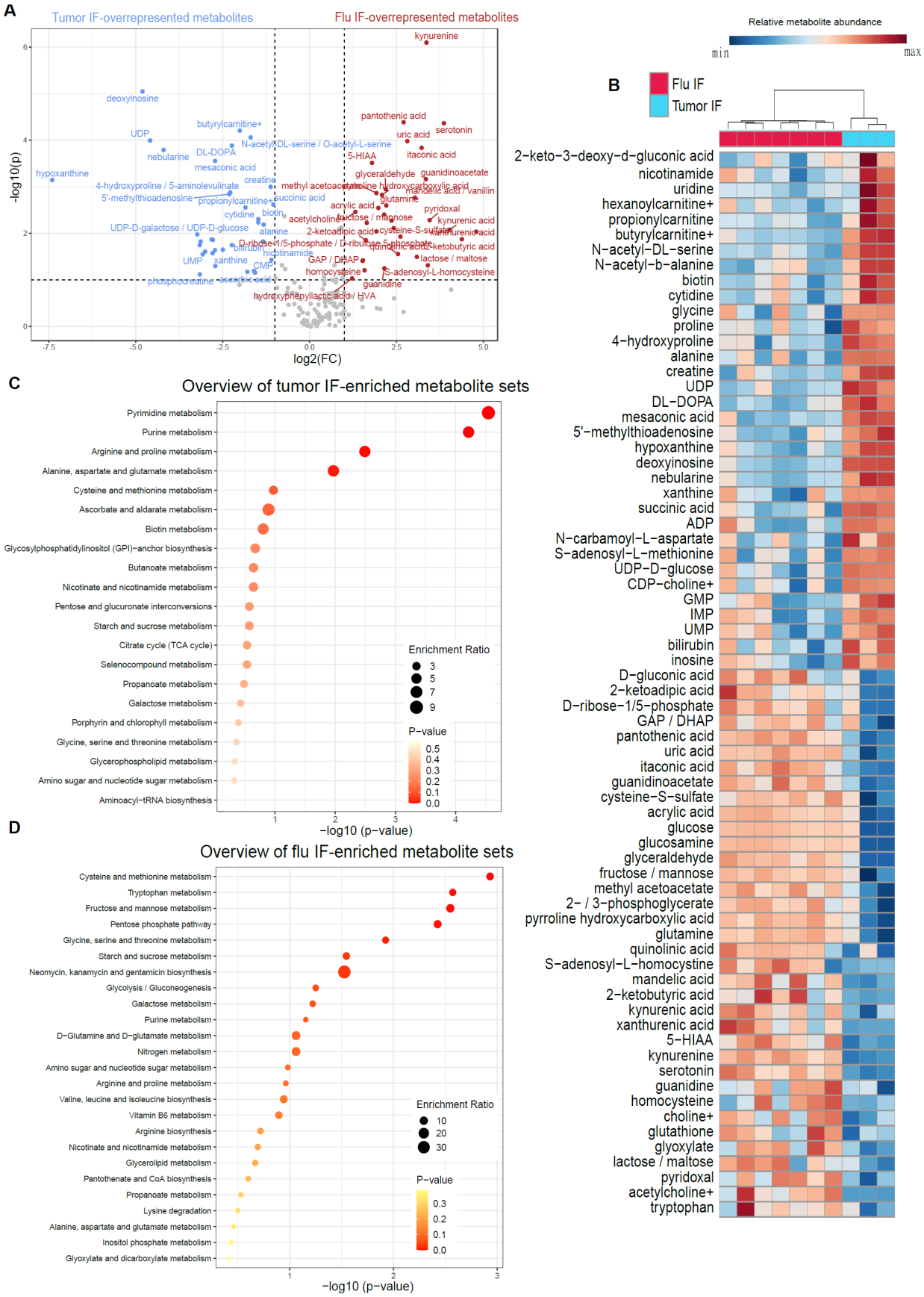

Supplemental Figure 6. Comparison of tumor interstitial fluid and influenza virus-infected lung interstitial fluid metabolite abundance. (**A**) Volcano plot of abundance of metabolites detected in

tumor (n=3) interstitial fluid (IF) and influenza virus-infected lung (flu, n=7) IF. Features with $p < 0.1$ were noted in red if $\log_2$(fold-change) ≥ 1.5 or blue if $\log_2$(fold-change) ≤ -1.5 when comparing flu IF versus tumor IF. (**B**) Heatmap of top 50 differentially represented metabolites between flu IF and tumor IF. (**C**) Overrepresentation analysis of significantly ($p < 0.1$) overrepresented metabolites in tumor IF relative to flu IF (**D**) Overrepresentation analysis of significantly ($p < 0.1$) overrepresented metabolites in flu IF relative to tumor IF.

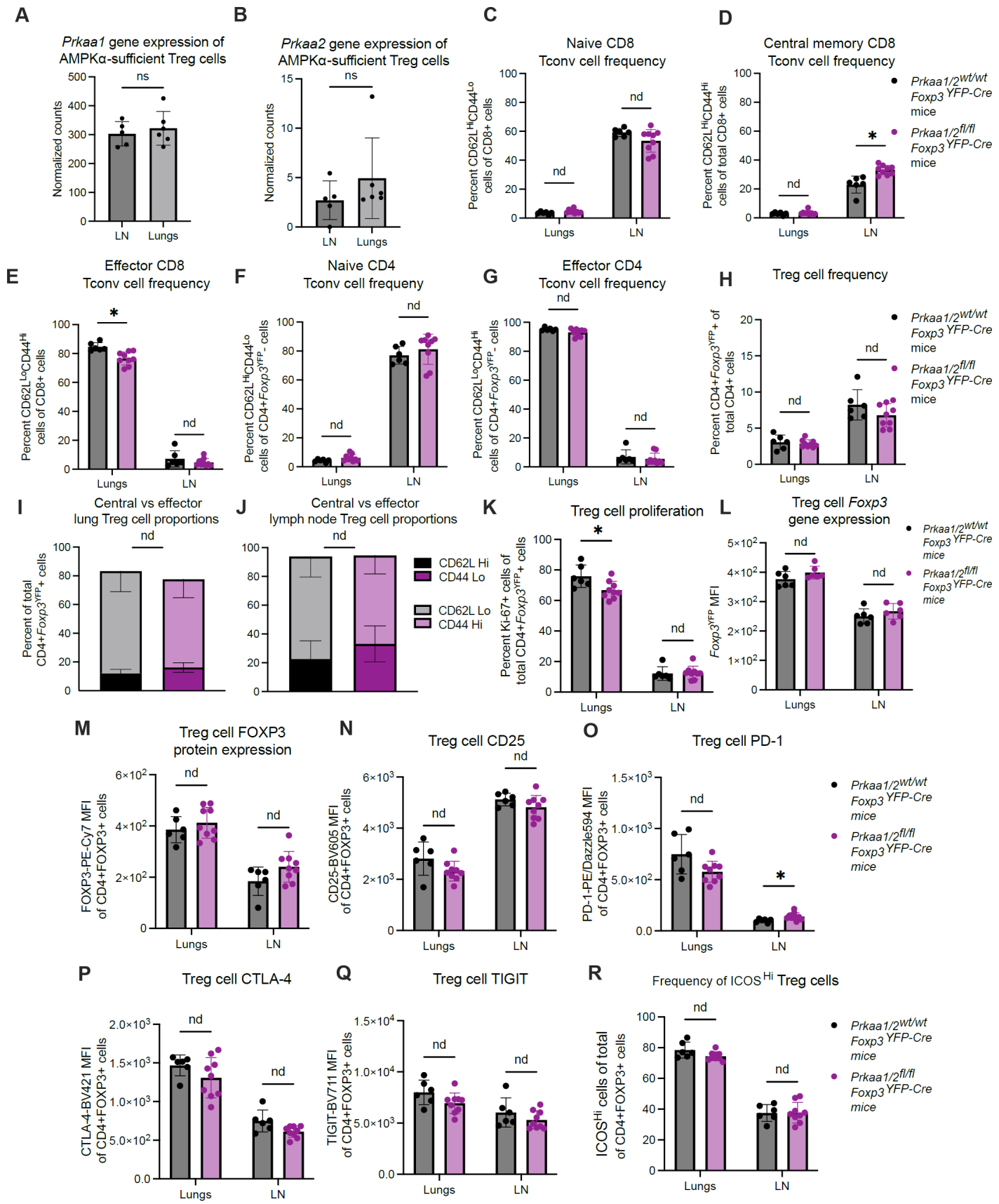

Supplemental Figure 7. Phenotyping of AMPKα-sufficient and -deficient Treg cells in the lung during viral pneumonia. (**A-B**) Normalized gene expression counts of *Prkaa1* (A) and *Prkaa2* (B) in

CD4+*Foxp3*^{YFP}+ cells sorted from axillary lymph nodes (LN; *n*=5) and lungs (*n*=6) of *Prkaa1/2*$^{wt/wt}$*Foxp3*$^{YFP\text{-}Cre}$ (control) mice at day 10 following intra-tracheal inoculation of influenza A/WSN/33 H1N1 (influenza) virus. (**C-E**) Frequency of naive (CD62L^{Hi}CD44^{Lo}; C), central memory (CD62L^{Hi}CD44^{Hi}; D), and effector (CD62L^{Lo}CD44^{Hi}; E) CD8+ conventional T (Tconv) cells out of total CD8+ cells in lungs and LN (*n*=6 control, *n*=9 *Prkaa1/2*$^{fl/fl}$*Foxp3*$^{YFP\text{-}Cre}$ mice) at day 10 post-influenza virus inoculation. (**F-G**) Frequency of naive (F) and effector (G) CD4+ Tconv cells out of total CD4+*Foxp3*^{YFP}- cells in lungs and LN (*n*=6 control, *n*=9 *Prkaa1/2*$^{fl/fl}$*Foxp3*$^{YFP\text{-}Cre}$ mice) at day 10 post-influenza virus inoculation. (**H**) Frequency of CD4+*Foxp3*^{YFP}+ cells out of total CD4+ cells in lungs and LN (*n*=6 control, *n*=9 *Prkaa1/2*$^{fl/fl}$*Foxp3*$^{YFP\text{-}Cre}$ mice) at day 10 post-influenza virus inoculation. (**I-J**) Frequency of central (CD62L^{Hi}CD44^{Lo}) and effector (CD62L^{Lo}CD44^{Hi}) CD4+*Foxp3*^{YFP}+ cells out of total CD4+Foxp3+ cells in lungs (I) and LN (J; *n*=6 control, *n*=9 *Prkaa1/2*$^{fl/fl}$*Foxp3*$^{YFP\text{-}Cre}$ mice) at day 10 post-influenza virus inoculation. (**K**) Frequency of Ki-67+CD4+*Foxp3*^{YFP}+ cells out of total CD4+*Foxp3*^{YFP}+ cells in lungs and LN (*n*=6 control, *n*=9 *Prkaa1/2*$^{fl/fl}$*Foxp3*$^{YFP\text{-}Cre}$ mice) at day 10 post-influenza virus inoculation. (**L**) *Foxp3*^{YFP} mean fluorescence intensity (MFI) of CD4+*Foxp3*^{YFP}+ cells in lungs and LN (*n*=6 control, *n*=6 *Prkaa1/2*$^{fl/fl}$*Foxp3*$^{YFP\text{-}Cre}$ mice) at day 10 post-influenza virus inoculation. (**M-Q**) FOXP3-PE-Cy7 (M), CD25-BV605 (N), PD-1-PE/Dazzle594 (O), CTLA-4-BV421 (P) and TIGIT-BV711 (Q) MFI of CD4+FOXP3+ cells from lungs and LN (*n*=6 control, *n*=9 *Prkaa1/2*$^{fl/fl}$*Foxp3*$^{YFP\text{-}Cre}$) at day 10 post-influenza virus inoculation. (**R**) Frequency of ICOS^{Hi} CD4+FOXP3+ cells of total CD4+FOXP3+ cells in lungs and LN (*n*=6 control, *n*=9 *Prkaa1/2*$^{fl/fl}$*Foxp3*$^{YFP\text{-}Cre}$) at day 10 post-influenza virus inoculation. * $q < 0.05$, ns not significant, nd no discovery according to Mann Whitney U test (A-B) with two-stage linear step-up procedure of Benjamini, Krieger, and Yekutieli with Q = 5% (C-R).

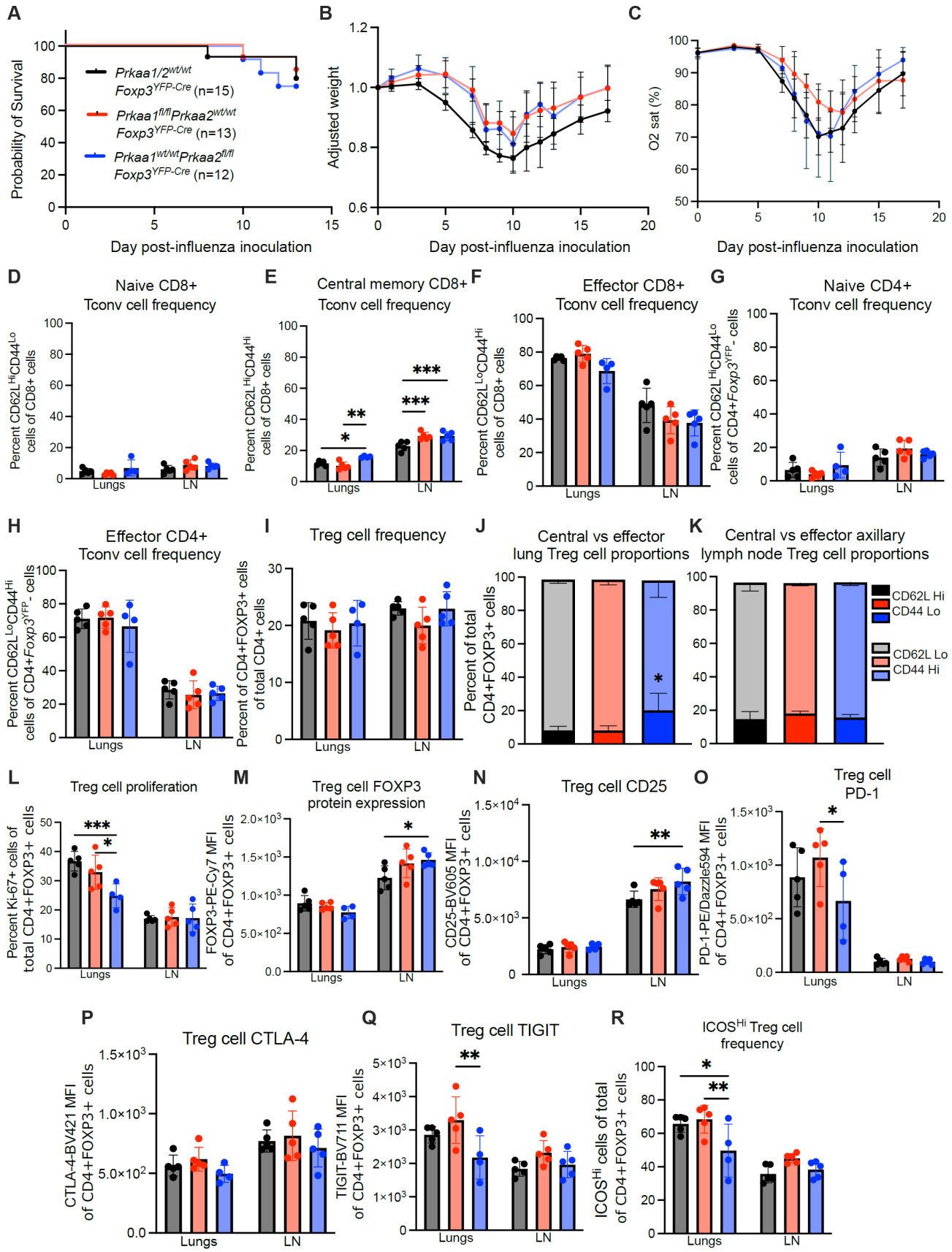

Supplemental Figure 8. Phenotyping of AMPKα1/2-sufficient, α1-deficient, and α2-deficient Treg cells in the lung during viral pneumonia. (**A**) Survival of control (*n*=8), *Prkaa1*$^{fl/fl}$*Foxp3*$^{YFP\text{-}Cre}$ (*n*=7),

and *Prkaa2*$^{fl/fl}$*Foxp3*$^{YFP\text{-}Cre}$ (*n*=6) mice following intra-tracheal inoculation of 12.5 plaque forming units (PFUs) of influenza A/WSN/33 H1N1 (influenza) virus. (**B**-**C**) Weight (B), and arterial oxyhemoglobin saturation (C) over time of control (*n*=6), *Prkaa1*$^{fl/fl}$*Foxp3*$^{YFP\text{-}Cre}$ (*n*=3), and *Prkaa2*$^{fl/fl}$*Foxp3*$^{YFP\text{-}Cre}$ (*n*=5) mice following intra-tracheal inoculation of 12.5 PFUs of influenza virus. (**D**-**F**) Frequency of naive (CD62L^{Hi}CD44^{Lo}; D), central memory (CD62L^{Hi}CD44^{Hi}; E), and effector (CD62L^{Lo}CD44^{Hi}; F) CD8+ conventional T (Tconv) cells out of total CD8+ cells in lungs and axillary lymph nodes (LN). (**G**-**H**) Frequency of naive (G) and effector (H) CD4+ Tconv cells out of total CD4+*Foxp3*^{YFP}- cells in lungs and LN. (**I**) Frequency of CD4+FOXP3+ cells out of total CD4+ cells in lungs and LN. (**J**-**K**) Frequency of central (CD62L^{Hi}CD44^{Lo}) and effector (CD62L^{Lo}CD44^{Hi}) CD4+FOXP3+ cells out of total CD4+FOXP3+ cells in lungs (J) and LN (K). * $p < 0.05$ versus control and *Prkaa1*$^{fl/fl}$*Foxp3*$^{YFP\text{-}Cre}$. (**L**) Frequency of Ki-67+CD4+FOXP3+ cells out of total CD4+FOXP3+ cells in lungs and LN. (**M**-**Q**) FOXP3-PE-Cy7 (M), CD25-BV605 (N), PD-1-PE/Dazzle594 (O), CTLA-4-BV421 (P) and TIGIT-BV711 (Q) MFI of CD4+FOXP3+ cells from lungs and LN. (**R**) Frequency of ICOS^{Hi} CD4+FOXP3+ cells of total CD4+FOXP3+ cells in lungs and LN. For D-R, *n*=5 lungs and LN for control mice, *n*=5 lungs and LN for *Prkaa1*$^{fl/fl}$*Foxp3*$^{YFP\text{-}Cre}$ mice, and *n*=4 lungs, *n*=5 LN for *Prkaa2*$^{fl/fl}$*Foxp3*$^{YFP\text{-}Cre}$ mice at day 10 post-influenza virus inoculation. Survival curve (A) *p* was determined using log-rank (Mantel-Cox) test. * $q < 0.05$, ** $q < 0.01$, *** $q < 0.001$, according to Mann Whitney U test with two-stage linear step-up procedure of Benjamini, Krieger, and Yekutieli with Q = 5% (B-R).

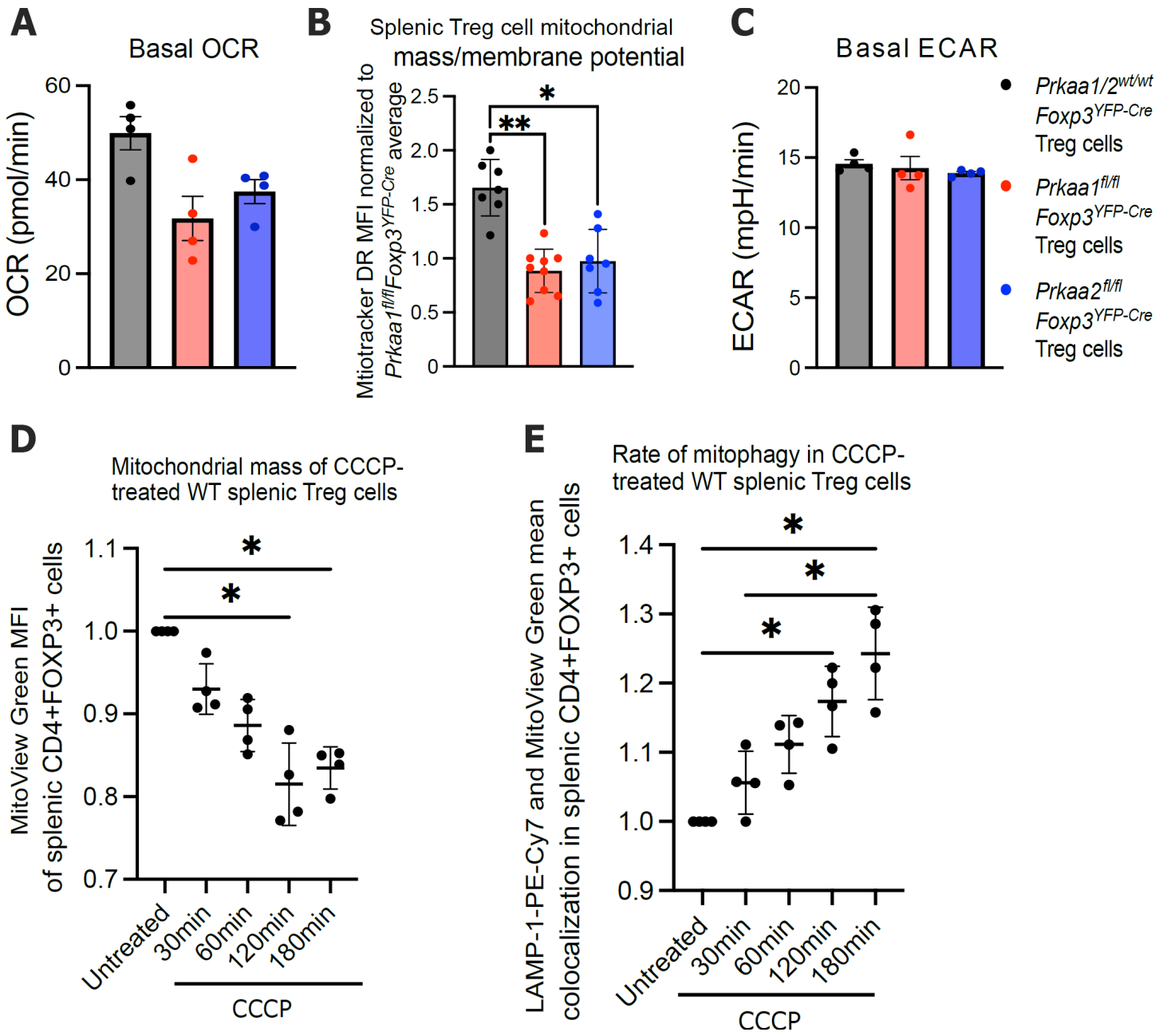

Supplemental Figure 9. Metabolic phenotyping of AMPKα1/2-sufficient, α1-deficient, and α2-deficient splenic Treg cells at homeostasis. (**A**) Basal oxygen consumption rate (OCR) of CD4+*Foxp3*^{YFP}+ splenocytes from control (*n*=4), *Prkaa1*$^{fl/fl}$*Foxp3*$^{YFP\text{-}Cre}$ (*n*=4), and *Prkaa2*$^{fl/fl}$*Foxp3*$^{YFP\text{-}Cre}$ (*n*=4) mice. (**B**) MitoTracker Deep Red (DR) mean fluorescence intensity (MFI) of CD4+*Foxp3*^{YFP}+ splenocytes at homeostasis (*n*=7 control, *n*=9 *Prkaa1*$^{fl/fl}$*Foxp3*$^{YFP\text{-}Cre}$, *n*=7 Prkaa2$^{fl/fl}$*Foxp3*$^{YFP\text{-}Cre}$ mice). Data normalized to *Prkaa1*$^{fl/fl}$*Foxp3*$^{YFP\text{-}Cre}$ mice average across three independent experiments. (**C**) Basal extracellular acidification rate (ECAR) of CD4+*Foxp3*^{YFP}+ splenocytes (*n*=4 control, *n*=4 *Prkaa1*$^{fl/fl}$*Foxp3*$^{YFP\text{-}Cre}$, *n*=4 Prkaa2$^{fl/fl}$*Foxp3*$^{YFP\text{-}Cre}$ mice). (**D-E**) MitoView Green MFI (D) and mean LAMP-1-PE-Cy-7/MitoView Green co-localization (E) over time of CD4+FOXP3+ splenocytes from control mice (*n*=4) after in vitro exposure to CCCP (10 μM); data were normalized to untreated condition. * $p < 0.05$, ** $p < 0.01$ according to Kruskal-Wallis test with two-stage linear step-up procedure of Benjamini, Krieger, and Yekutieli with Q = 5%.

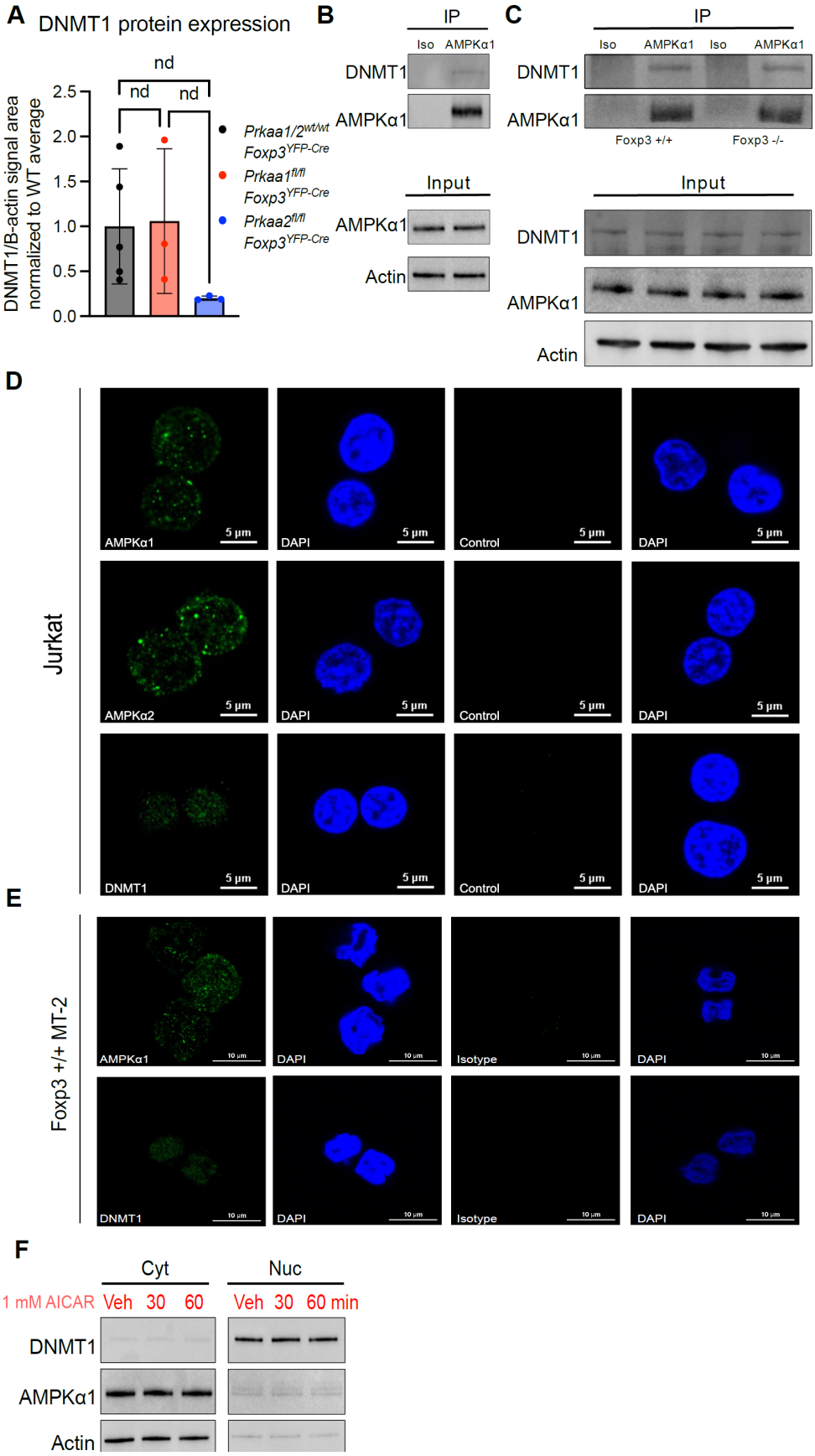

Supplemental Figure 10. AMPKα1 interacts with DNMT1 in Jurkat and MT-2 cells. (**A**) DNMT1 protein expression of splenic CD4+*Foxp3*^{YFP}+ (Treg) cells at homeostasis (*n*=5 control, *n*=3

177 *Prkaa1*$^{fl/fl}$*Foxp3*$^{YFP\text{-}Cre}$, *n*=3 *Prkaa2*$^{fl/fl}$*Foxp3*$^{YFP\text{-}Cre}$). Data from controls also shown in Figure 6D. DNMT1
178 peak intensity area was normalized to the corresponding sample's β-actin peak intensity area. (**B**-**C**)
179 anti-AMPKα1 and isotype control immunoprecipitates from Jurkat cell (B) and MT-2 cell (C) lysates
180 blotted for DNMT1 protein. (**D**-**E**) Representative microscopy images of Jurkat cells (D) and MT-2 cells
181 (E) showing AMPKα1 and DNMT1 subcellular localization. (**F**) Immunoblots for DNMT1, AMPKα1, and
182 β-actin on nuclear and cytoplasmic fractions of cell lysates obtained from AMPKα1/α2-sufficient ex vivo-
183 induced (i)Treg cells treated with either vehicle, 30min AICAR 1mM, or 60min AICAR 1mM. nd no
184 discovery according to Mann-Whitney *U* test with two-stage linear step-up procedure of Benjamini,
185 Krieger, and Yekutieli with Q = 5% (A).
186

187

188 **Supplemental File 1.** Peak intensity data of annotated metabolites detected in AMPKα1/α2-deficient
189 and -sufficient splenic Treg cells of 12–15-week-old mice at homeostasis.
190
191 **Supplemental File 2.** Differentially expressed genes detected when comparing AMPKα1/α2-deficient
192 versus -sufficient splenic Treg cells of 12–15-week-old mice at homeostasis and their corresponding
193 k-means cluster.
194
195 **Supplemental File 3.** Differentially expressed genes detected when comparing AMPKα1/α2-deficient
196 versus -sufficient B16 melanoma tumor-infiltrating Treg cells of 12–15-week-old mice (15 days after
197 subcutaneous engraftment) and their corresponding k-means cluster.
198
199 **Supplemental File 4.** Differentially expressed genes detected when comparing AMPKα1/α2-deficient
200 versus -sufficient B16 melanoma tumor-infiltrating Treg cells of 12–15-week-old mice (12 days after
201 subcutaneous engraftment) and their corresponding k-means cluster.
202
203 **Supplemental File 5.** Differentially expressed genes detected when comparing AMPKα1-deficient
204 versus -sufficient B16 melanoma tumor-infiltrating Treg cells of 12–15-week-old mice (12 days after
205 subcutaneous engraftment) and their corresponding k-means cluster.
206
207 **Supplemental File 6.** Differentially expressed genes detected when comparing AMPKα2-deficient
208 versus -sufficient B16 melanoma tumor-infiltrating Treg cells of 12–15-week-old mice (12 days after
209 subcutaneous engraftment) and their corresponding k-means cluster.
210
211 **Supplemental File 7.** Peak intensity data of annotated metabolites detected in the interstitial fluid of
212 lungs from influenza virus-infected mice (10 days post-inoculation), the interstitial fluid of B16
213 melanoma tumors (15 days after subcutaneous engraftment), and paired plasma samples.
214
215 **Supplemental File 8.** Peak intensity data of annotated metabolites detected in AMPKα1/α2-deficient
216 and -sufficient lung Treg cells from 12–15-week-old influenza virus-infected mice (10 days post-
217 inoculation).
218